European Journal of Mechanics A/Solids 51 (2015) 123–139

Contents lists available at ScienceDirect

European Journal of Mechanics A/Solids

journal homepage: www.elsevier.com/locate/ejmsol

Thermo-mechanical fracture study of inhomogeneous cracked solids by the extended isogeometric analysis method

H. Bayesteh, A. Afshar, S. Mohammdi*

School of Civil Engineering, College of Engineering, University of Tehran, Tehran, Iran

ARTICLE INFO

Article history:
Received 6 January 2014
Accepted 9 December 2014
Available online 18 December 2014

Keywords:
Extended isogeometric analysis (XIGA)
Inhomogeneous material
Thermo-mechanical loading

ABSTRACT

The extended isogeometric analysis method (XIGA) is further developed to study fracture of homogeneous and inhomogeneous materials under mechanical and thermo-mechanical loadings. The domain of the problem is discretized by the knot spans of the isogeometric analysis (IGA) and the same basis functions used for constructing the geometry are employed to discretize the solution. In addition, crack face discontinuity and tip enrichment functions of the extended finite element method (XFEM) are incorporated into the NURBS basis functions of IGA in order to reproduce crack face displacement discontinuity and tip singularity of the stress field. The proper form of the interaction integral method in inhomogeneous materials and thermal conditions is employed to evaluate the mixed mode stress intensity factors. In order to assess the efficacy of the proposed approach, a number of problems with different configurations and loadings are analyzed and the results are verified by comparing with the reference values.

1. Introduction

Manufacture of composites and other high-tech materials such as functionally graded materials (FGMs) has become increasingly sophisticated, and the area of their application incorporated more aspects of engineering. As a result, extensive research has been directed towards the study of their failure and fracture modes as the presence of cracks can adversely affect their structural and thermal safety and performance.

Practical fracture mechanics problems, which contain complex characteristics such as arbitrary geometries and loadings, and nonlinear material behavior, have limited the applicability of analytical methods (Lekhnitskii, 1963; Sih et al., 1965; Bowie and Freese, 1972; Kuo and Bogy, 1974; Viola et al., 1989; Lim et al., 2001; Nobile and Carloni, 2005) and directed many researchers to adopt advanced numerical methods, such as the finite element method (FEM), the boundary element method (BEM), meshless methods, and the extended finite element method.

In XFEM (Melenk and Babuska, 1996; Belytschko and Black, 1999), cracks are not required to conform to element edges and they are modeled by adding enrichment functions, derived from asymptotic analytical solutions, to the classical finite element shape functions. As a result, the enriched basis becomes capable of reproducing the crack face displacement discontinuity and complex crack tip stress fields, without the necessity of using singular elements or remeshing procedure in crack propagation problems (Sukumar et al., 2003; Sukumar et al., 2000, 2001; Dolbow, 1999; Stolarska et al., 2001; Moës et al., 2002; Mohammadi, 2008, 2012). Since the seminal work of Belytschko and Black (1999), XFEM has been widely used for modeling different discontinuity problems (Belytschko et al., 2009). Moreover, for the specific applications of fracture analysis of composites, new enrichment functions have been proposed to capture crack tip singularity; including static orthotropic function (Asadpoure et al., 2006a; Asadpoure and Mohammadi, 2007; Asadpoure et al., 2006b), dynamic orthotropic problems (Motamedi and Mohammadi, 2010a, 2010b), and anisotropic bi-material delamination (Ashari and Mohammadi, 2011; Menk and Bordas, 2010; Ashari and Mohammadi, 2012).

Trying to bridge the gap between design and analysis, Hughes et al. (2005) proposed the Isogeometric Analysis (IGA) as an alternative to FEM. The original idea is to use Non-Uniform Rational B-spline (NURBS), a technology used in computer graphics for free form modeling, as a basis for analysis. In other words, NURBS functions in IGA both define the exact geometry and

* Corresponding author. High Performance Computing Lab, School of Civil Engineering, University of Tehran, Tehran, Iran. Tel.: +98 21 6111 2258; fax: +98 21 6640 3808.
E-mail address: smoham@ut.ac.ir (S. Mohammdi).

http://dx.doi.org/10.1016/j.euromechsol.2014.12.004
0997-7538/

estimate the solution (Hughes et al., 2005). IGA has been successfully used in many engineering problems: shape optimization (Wall et al., 2008; Qian and Sigmund, 2011; Qian, 2010; Manh et al., 2011), shell analysis (Uhm and Youn, 2009; Kiendll et al., 2009; Benson et al., 2010, 2011; Casanova and Gallego, 2013), FGM and laminated composite plates (Valizadeh et al., 2013; Tran Loc et al., 2013; Thai Chien et al., 2012; Thai Chien et al., 2013; Thai Chien et al., 2013; Nguyen-Xuan et al., 2013; Tran et al., 2013), contact mechanics (Temizer et al., 2011, 2012; Jia, 2011; De Lorenzis et al., 2011), and so forth. Recently, IGA has been extended to tackle fracture problems by Ghorashi et al. (2012) and De Luycker et al. (2011) in the form of extended isogeometric analysis (XIGA), incorporating the enrichment technique of XFEM into IGA to model crack face discontinuity and crack tip singular stress field. Nevertheless, the problems solved by XIGA have remained limited to homogenous solids under mechanical loading. Here, the XIGA approach (Ghorashi et al., 2012) is further developed to include FGM composites and thermo-mechanical loadings for both isotropic and orthotropic materials.

A number of researchers have already studied cracked FGM by employing different approaches: experimental methods (El-Hadek and Tippur, 2003a, 2003b; Yao et al., 2005), numerical and analytical methods (Delale and Erdogan, 1983; Abotula et al., 2012; Gupta et al., 2012; Schovanec and Walton, 1988; Konda and Erdogan, 1994; Gu and Asaro, 1997; Erdogan and Wu, 1997; Jin et al., 2002; Kim and Paulino, 2005, 2003, 2002). Specifically, Hosseini et al. (2013) and Bayesteh and Mohammadi (2013) used XFEM to analyze fracture of FGMs under thermo-mechanical and mechanical loadings, respectively. Furthermore, several researchers also utilized numerical methods to study fracture of cracked solids under thermal loadings: finite and boundary elements (Wilson and Yu, 1979; Shih et al., 1986; Raveendra and Banerjee, 1992; Prasad et al., 1994a,b), and XFEM (Merle and Dolbow, 2002). To the best knowledge of the authors, however, it is the first time that XIGA is applied to fracture analysis of either FGM composites or thermal loadings.

This paper is organized as follows: Section 2 is devoted to the basics and formulation of isogeometric analysis. Then, XIGA crack modeling procedure and computation of stress intensity factors for cracks in FGM solids under thermal loading are presented in Section 3. Several numerical examples with different configurations are solved in Section 4 in order to evaluate the efficiency of XIGA in thermo-mechanical fracture analysis of homogeneous and inhomogeneous isotropic/orthotropic problems. Finally, Section 5 closes this paper with a conclusion.

2. B-splines and NURBS

A one-dimensional Knot vector $\Xi = \{\xi_1, \xi_2, \ldots, \xi_{n+p+1}\}$ is a non-decreasing parametric representation of coordinates in the parametric space, where ξ_i is the i^{th} knot and n indicates the number of basis functions of order p. Knots divide the parametric space into knot spans, where numerical integrations are implemented. With respect to a given knot vector, the B-spline basis function of orders $p = 0$ and higher orders ($p > 0$) are defined as (Cox, 1971; De Boor, 1972; Cottrell et al., 2009),

$$N_{i,0}(\xi) = \begin{cases} 1 & \text{if } \xi_i \le \xi \le \xi_{i+1} \\ 0 & \text{otherwise} \end{cases} \tag{1}$$

$$N_{i,p}(\xi) = \frac{\xi - \xi_i}{\xi_{i+p} - \xi_i} N_{i,p-1}(\xi) + \frac{\xi_{i+p+1} - \xi}{\xi_{i+p+1} - \xi_{i+1}} N_{i+1,p-1}(\xi) \tag{2}$$

To further generalize the representation of B-spline piecewise polynomials, the Non-uniform Rational B-Spline (NURBS) has been introduced by multiplying B-spline basis functions with appropriate weights

$$R_{i,p}(\xi) = \frac{N_{i,p}(\xi) w_i}{W_i} = \frac{N_{i,p}(\xi) w_i}{\sum_{j=1}^{n} N_{i,p}(\xi) w_j} \tag{3}$$

where $N_{i,p}$ is the i^{th} basis function of order p, and w_i are a set of n positive weights. In a manner similar to B-spline curves, NURBS curves are constructed from linear combination of NURBS basis functions:

$$\mathbf{C}(\xi) = \sum_{i=1}^{n} R_{i,p}(\xi) \mathbf{B}_i \tag{4}$$

Having control points $\mathbf{B}_{i,j}$ and two knot vectors $\Xi = \{\xi_1, \xi_2, \ldots, \xi_{n+p+1}\}$ and $\Theta = \{\eta_1, \eta_2, \ldots, \eta_{m+q+1}\}$ in a Bi-dimensional space, a tensor-product NURBS surface is defined as

$$\mathbf{S}(\xi, \eta) = \sum_{i-1}^{n} \sum_{j-1}^{m} R_{i,j}^{p,q}(\xi, \eta) \mathbf{B}_{i,j} \tag{5}$$

where $\mathbf{B}_{i,j}$ are the control points in a bi-dimensional space. The bivariate NURBS basis functions$R_{i,j}^{p,q}$ are similarly defined as,

$$R_{i,j}^{p,q}(\xi, \eta) = \frac{N_{i,p}(\xi) M_{j,q}(\eta) w_{i,j}}{\sum_{a=1}^{n} \sum_{b=1}^{m} M_{b,q}(\eta) N_{a,p}(\xi) w_{a,b}} \tag{6}$$

where $w_{i,j}$ are a set of $n \times m$ positive weights. Typical two dimensional basis functions with different orders of continuity are presented in Fig. 1.

3. Isogeometric formulation

3.1. Problem statement

Let us consider the problem of a linear elastic solid with a crack, as shown in Fig. 2. In the present study, both homogeneous and FGM solids under mechanical and thermal loadings are considered. Under the mechanical loading, the solution of the problem must satisfy the following equilibrium and boundary conditions

$$\text{div}(\boldsymbol{\sigma}) + \mathbf{f} = 0 \quad \text{In } \Omega \tag{7}$$

$$\boldsymbol{\sigma} \cdot \mathbf{n} = \overline{\boldsymbol{\sigma}} \quad \text{On } \Gamma_t \tag{8}$$

$$\mathbf{u} = \overline{\mathbf{u}} \quad \text{On } \Gamma_u \tag{9}$$

where $\boldsymbol{\sigma}, \boldsymbol{f}, \boldsymbol{u}, \overline{\boldsymbol{\sigma}}, \overline{\mathbf{u}}$, and $\boldsymbol{n}$ are the stress, body force, displacement, prescribed traction on the natural boundary Γ_t, prescribed displacement on the essential boundary Γ_u, and the unit normal outward vector, respectively. Under the thermal loading, the two-dimensional orthotropic steady state heat conduction with its boundary conditions is solved

$$\nabla \cdot (\mathbf{k} \nabla T) = 0 \tag{10}$$

$$T = \overline{T} \quad \text{On } \Gamma_T \tag{11}$$

$$\mathbf{q} = \overline{\mathbf{q_n}} \quad \text{On } \Gamma_q \tag{12}$$

where $\mathbf{k}$ denotes the vector of heat conductivity coefficient along the i direction, T is the temperature on each point, $\overline{T}$ is the prescribed temperature, and $\overline{\mathbf{q_n}}$ is the prescribed value of the heat flux.

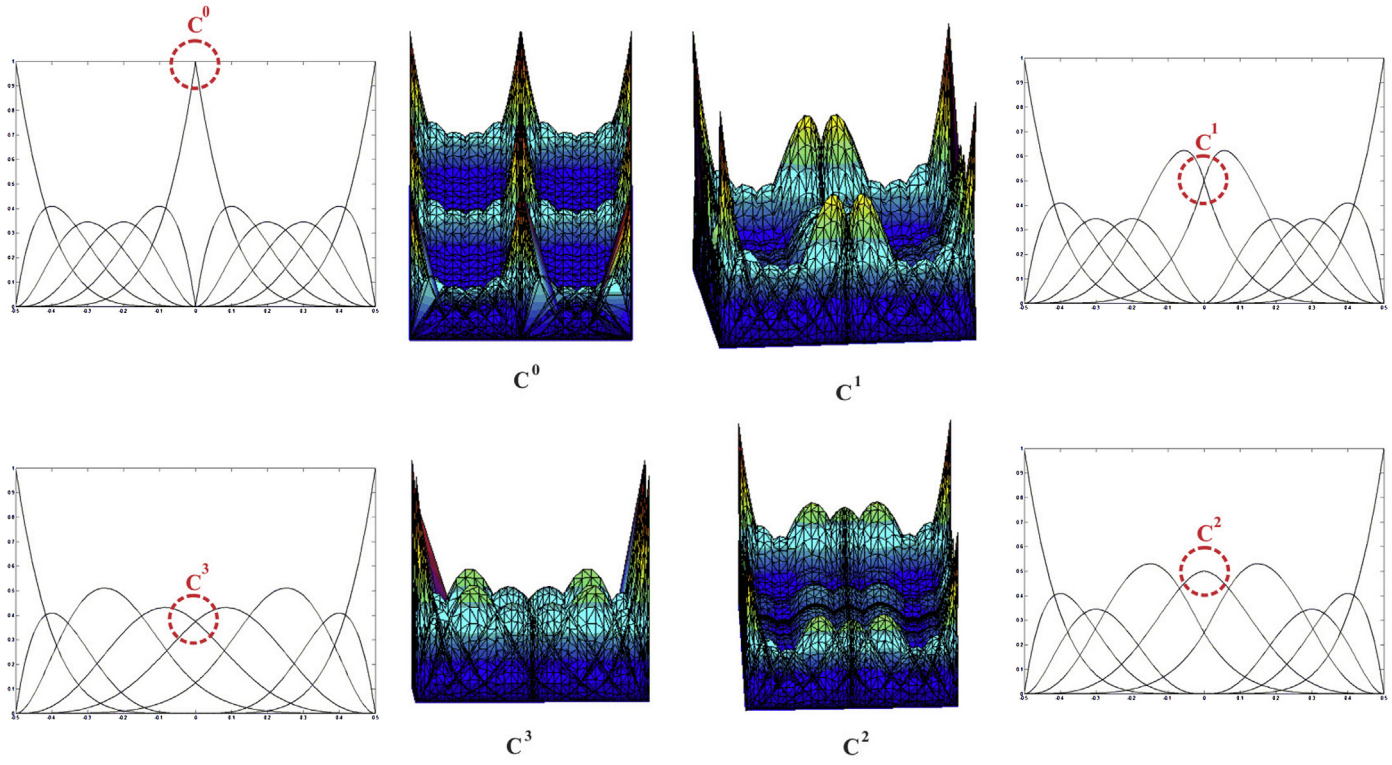

Fig. 1. Different orders of continuity for a quartic B-spline.

The crack is deemed to be insulated in this work, resulting in a discontinuity in the temperature field across crack faces.

3.2. Stress–strain relationship

The strain in a thermo-mechanical problem is composed of two parts

$$\boldsymbol{\varepsilon}^{\mathrm{t}} = \boldsymbol{\varepsilon}^{\mathrm{m}} + \boldsymbol{\varepsilon}^{\mathrm{th}} \tag{13}$$

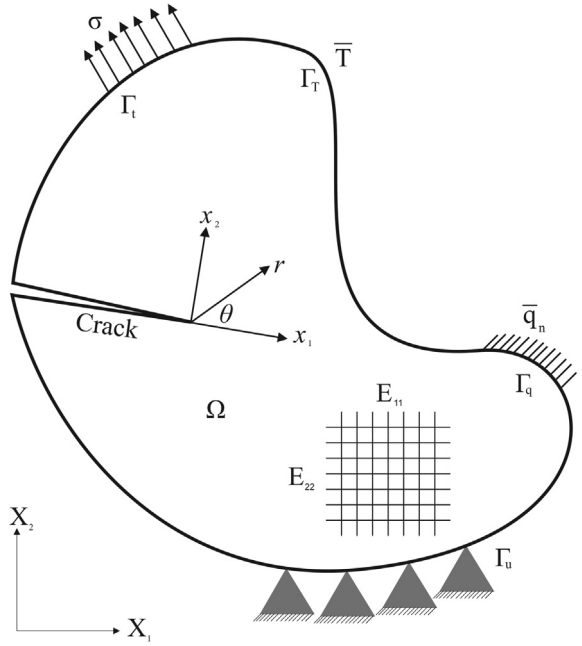

Fig. 2. An arbitrary cracked two-dimensional medium.

where $\boldsymbol{\varepsilon}^{\mathrm{t}}$, $\boldsymbol{\varepsilon}^{\mathrm{m}}$, and $\boldsymbol{\varepsilon}^{\mathrm{th}}$ are the total, mechanical and thermal strains, respectively.

The thermal part of the strain $\varepsilon^{\mathrm{th}}$ for the plane stress state can be written as

$$\begin{Bmatrix} \varepsilon_{11}^{\mathrm{th}} \\ \varepsilon_{22}^{\mathrm{th}} \\ \varepsilon_{33}^{\mathrm{th}} \\ 2\varepsilon_{12}^{\mathrm{th}} \end{Bmatrix} = \begin{Bmatrix} \alpha_{11} \\ \alpha_{22} \\ \alpha_{33} \\ 0 \end{Bmatrix} \Delta T \tag{14}$$

and for plane strain

$$\begin{Bmatrix} \varepsilon_{11}^{\mathrm{th}} \\ \varepsilon_{22}^{\mathrm{th}} \\ \varepsilon_{33}^{\mathrm{th}} \\ 2\varepsilon_{12}^{\mathrm{th}} \end{Bmatrix} = \begin{Bmatrix} \nu_{31}\alpha_{33} + \alpha_{11} \\ \nu_{32}\alpha_{33} + \alpha_{22} \\ \alpha_{33} \\ 0 \end{Bmatrix} \Delta T \tag{15}$$

where ν_{ij} and α_{ij} denote the Poison's ratio and the thermal expansion coefficient, respectively.

Based on the generalized Hook's law (Lekhnitskii, 1963), $\boldsymbol{\varepsilon}^{\mathrm{m}}$, the mechanical part of the strain, can be written as,

$$\begin{bmatrix} \varepsilon_{11}^{\mathrm{m}} \\ \varepsilon_{22}^{\mathrm{m}} \\ \varepsilon_{33}^{\mathrm{m}} \\ 2\varepsilon_{23}^{\mathrm{m}} \\ 2\varepsilon_{13}^{\mathrm{m}} \\ 2\varepsilon_{12}^{\mathrm{m}} \end{bmatrix} = \begin{bmatrix} a_{11} & a_{12} & a_{13} & a_{14} & a_{15} & a_{16} \\ & a_{22} & a_{23} & a_{24} & a_{25} & a_{26} \\ & & a_{33} & a_{34} & a_{35} & a_{36} \\ & & & a_{44} & a_{45} & a_{46} \\ & \text{SYM.} & & & a_{55} & a_{56} \\ & & & & & a_{66} \end{bmatrix} \begin{bmatrix} \sigma_{11} \\ \sigma_{22} \\ \sigma_{33} \\ \sigma_{23} \\ \sigma_{13} \\ \sigma_{12} \end{bmatrix} \tag{16}$$

For a plane strain state, however, $a_{\alpha\beta}$ should be replaced by $b_{\alpha\beta}$

$$b_{\alpha\beta} = a_{\alpha\beta} - \frac{a_{\alpha 3}a_{\beta 3}}{a_{33}} \quad (\alpha, \beta = 1, 2, 6) \tag{17}$$

3.3. XIGA discretization

The discretized form of the mechanical equation (Eq. (7)) can be written as

$$\mathbf{K}\mathbf{u}^{\mathrm{h}} = \mathbf{f} \tag{18}$$

where the displacement vector $\mathbf{u}^{\mathrm{h}}$ consists of both standard and additional degrees of freedom (Mohammadi, 2008)

$$\mathbf{u}^{\mathrm{h}} = \{\, \mathbf{u} \quad \mathbf{a} \quad \mathbf{b}_1 \quad \mathbf{b}_2 \quad \mathbf{b}_3 \quad \mathbf{b}_4 \,\} \tag{19}$$

where $\mathbf{u}^{\mathrm{h}}$ denotes the standard degrees of freedom while $\mathbf{a}$ and $\mathbf{b}_\alpha$ ($\alpha = 1,2,3,$ and 4) denote additional degrees of freedom used to reproduce crack faces and crack tip fields, respectively. The global stiffness matrix $\mathbf{K}$ and the mechanical force vector $\mathbf{f}$ are all formed by the assembly of their element contributions (Mohammadi, 2008)

$$\mathbf{K}_{ij}^{e} = \begin{bmatrix} \mathbf{K}_{ij}^{ab} & \mathbf{K}_{ij}^{ua} & \mathbf{K}_{ij}^{ub} \\ \mathbf{K}_{ij}^{au} & \mathbf{K}_{ij}^{aa} & \mathbf{K}_{ij}^{ab} \\ \mathbf{K}_{ij}^{bu} & \mathbf{K}_{ij}^{ba} & \mathbf{K}_{ij}^{bb} \end{bmatrix} \tag{20}$$

$$\mathbf{f}_i = \left\{ \mathbf{f}_i^{u} \quad \mathbf{f}_i^{a} \quad \mathbf{f}_i^{b_1} \quad \mathbf{f}_i^{b_2} \quad \mathbf{f}_i^{b_3} \quad \mathbf{f}_i^{b_4} \right\}^{\mathrm{T}} \tag{21}$$

Definitions of the components of Eqs. (20) and (21) are provided in Appendix A. Similarly, the discretized form of the thermal Eq. (10) can be written as

$$\mathbf{Q}\mathbf{T}^{\mathrm{h}} + \mathbf{f}^{\mathrm{th}} = 0 \tag{22}$$

where the definition of temperature vector $\mathbf{T}^{\mathrm{h}}$ is similar to Eq. (19)

$$\mathbf{T}^{\mathrm{h}} = \{\, \mathbf{u} \quad \mathbf{a} \quad \mathbf{b}_1 \,\} \tag{23}$$

Formation of the thermal stiffness matrix $\mathbf{Q}$ and the thermal force vector $\mathbf{f}^{\mathrm{th}}$ are also equivalent to Eqs. (20) and (21) with a different form of matrix of basis function derivatives

$$\mathbf{Q}_{ij}^{e} = \begin{bmatrix} \mathbf{Q}_{ij}^{ab} & \mathbf{Q}_{ij}^{ua} & \mathbf{Q}_{ij}^{ub} \\ \mathbf{Q}_{ij}^{au} & \mathbf{Q}_{ij}^{aa} & \mathbf{Q}_{ij}^{ab} \\ \mathbf{Q}_{ij}^{bu} & \mathbf{Q}_{ij}^{ba} & \mathbf{Q}_{ij}^{bb} \end{bmatrix} \tag{24}$$

$$\mathbf{f}_i^{\mathrm{th}-e} = \{\, \mathbf{f}_i^{\mathrm{th}-u} \quad \mathbf{f}_i^{\mathrm{th}-a} \quad \mathbf{f}_i^{\mathrm{th}-} b_1 \,\} \tag{25}$$

Definitions of the components of Eqs. (24) and (25) are also provided in Appendix A. Having solved the thermal Eq. (22), the thermal strain $\boldsymbol{\varepsilon}^{th}$ can be calculated by Eq. (14) or (15) from the temperature values. Afterward, the force vector in $\boldsymbol{KU} = \boldsymbol{f}$ can be expressed as

$$\boldsymbol{f} = \boldsymbol{f}^{th-equivalent} + \boldsymbol{f}^{mech.} = \int_{\Omega} B^{T} C \varepsilon^{th} d\Omega + \boldsymbol{f}^{mech.} \tag{26}$$

where the $\boldsymbol{B}$ matrix is defined by Eqs. A5-A8 (Appendix A).

Since in general IGA shape functions do not meet Kronecker delta property, the penalty method is utilized in this paper to impose essential boundary conditions.

3.4. Modeling cracks in XIGA

The extended isogeometric analysis employs the basic concepts of enrichments of XFEM within the framework of IGA. In XIGA, the extended displacement or temperature fields for both crack faces and crack tips are added to the standard IGA approximation

$$\chi = \chi^{\mathrm{IGA}} + \chi^{\mathrm{XIGA}} = \chi^{\mathrm{IGA}} + \chi^{\mathrm{tip}} + \chi^{\mathrm{heaviside}} \tag{27}$$

where χ represents either the temperature T or the displacement $\boldsymbol{U}$. The $\chi^{\mathrm{heaviside}}$ part of the enrichment is used to model the crack face strong discontinuity in both temperature and displacement fields and is defined as (Mohammadi, 2008)

$$\chi^{\mathrm{heaviside}} = \sum_{i \in n_s} N_i(\mathbf{x}) H(\mathbf{x}) \widehat{a}_i \tag{28}$$

where n_s is the set of control points enriched by the Heaviside function. The Heaviside function for a point located at the physical coordinate $\mathbf{X}$ is defined as (Mohammadi, 2008)

$$H(\mathbf{X}) = \begin{cases} +1 & \text{if } (\mathbf{X} - \mathbf{X}^{*}) \cdot \mathbf{e}_n > 0 \\ -1 & \text{otherwise} \end{cases} \tag{29}$$

where $\mathbf{X}^{*}$ is the coordinate of the closest point of the crack to the point $\mathbf{X}$ (Fig. 3).

The χ^{tip} part of the enrichment is used to reproduce the complex analytical crack tip field (Mohammadi, 2008)

$$\chi^{tip} = \sum_{i \in Tp} N_i(\mathbf{x}) \left(\sum_{k \in F} f_k(\mathbf{x}) \widehat{\mathbf{b}}_{ik} \right) \tag{30}$$

where Tp is the set of control points enriched by the set F of crack tip functions f_k. These functions are derived from the asymptotic solution and are unique to each set of problems. For an isotropic solid under static mechanical loading, the following four functions are used (Dolbow, 1999)

$$F(r,\theta) = \left\{ \sqrt{r}\sin\left(\frac{\theta}{2}\right), \sqrt{r}\cos\left(\frac{\theta}{2}\right), \sqrt{r}\sin(\theta)\sin\left(\frac{\theta}{2}\right), \sqrt{r}\sin(\theta)\cos\left(\frac{\theta}{2}\right) \right\} \tag{31}$$

where polar coordinates r and θ are measured from the crack tip (Fig. 2). Moreover, in the case of orthotropic materials, the following four functions have been proposed (Asadpoure et al., 2006a)

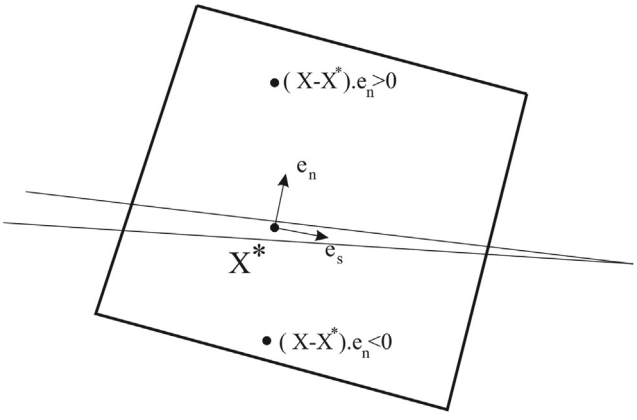

Fig. 3. Unit tangential and normal vectors.

$$F(r,\theta)=\left\{\sqrt{r}\cos\left(\frac{\theta_1}{2}\right)\sqrt{g_1(\theta)},\sqrt{r}\cos\left(\frac{\theta_2}{2}\right)\sqrt{g_2(\theta)},\right.$$
$$\left.\sqrt{r}\sin\left(\frac{\theta_1}{2}\right)\sqrt{g_1(\theta)},\sqrt{r}\sin\left(\frac{\theta_2}{2}\right)\sqrt{g_2(\theta)}\right\} \quad (32)$$

with

$$g_j(\theta)=\sqrt{\left(\cos(\theta)+\zeta_j\sin(\theta)\right)^2+\left(\beta_j\sin(\theta)\right)^2} \quad (j=1,2) \quad (33)$$

$$\theta_k(\theta)=\tan^{-1}\left(\frac{\beta_k\sin(\theta)}{\cos(\theta)+\zeta_k\sin(\theta)}\right) \quad (k=1,2) \quad (34)$$

where ζ_i and β_i are the real and complex parts of the roots of the characteristic equation (Lekhnitskii, 1963)

$$a_{11}^{tip}\mu^4-2a_{16}^{tip}\mu^3+\left(2a_{12}^{tip}+a_{66}^{tip}\right)\mu^2-2a_{26}^{tip}\mu+a_{22}^{tip}=0 \quad (35)$$

$$\mu_1=\zeta_1+i\beta_1$$
$$\mu_2=\zeta_2+i\beta_2 \quad (36)$$

where a_{ij} are defined by Eq. (16). It should be noted, however, that since no analytical solution exists in the literature for FGM solids, the homogeneous asymptotic solution with material properties evaluated at the crack tip is adopted for all FGM examples in this work.

For the thermal equation, the following tip enrichment is used (Duflot, 2008)

$$F^{th}(r,\theta)=\sqrt{r}\sin\left(\frac{\theta}{2}\right) \quad (37)$$

3.5. Determining the enriched control points

The method utilized in this paper for selecting the enriched control points is similar to the level set method used in XFEM with a slight difference stemmed from dissimilarities between the control points of XIGA, and nodes in XFEM. In the XFEM context, only nodes associated with elements containing either crack face or crack tips are enriched, whereas in an XIGA framework, many control points located far away from the crack may be enriched since their basis function influence domain is much larger, as illustrated in Fig. 4. A control point whose corresponding basis function has nonzero value in the crack face or crack tip is selected for enrichment with the Heaviside or tip enrichment functions, respectively. For instance in Fig. 4, all control points (located in the dashed rectangle) whose corresponding basis function has nonzero value in the crack tip knot span (blue rectangular domain (in web version)) are chosen to be enriched with crack tip enrichment functions in their influence domain.

A subtle yet important point is that for the control points, whose basis functions are nonzero over both knot spans containing the crack face and knot spans containing the crack tip, only the crack tip enrichment functions are used, since enriching these control points with the Heaviside function erroneously extends the crack front. Crack tip enrichments are capable of reproducing the jump across the exact crack face, and hence, the control points with theses enrichments do not alter the kinematic discontinuity of the real crack. The ability of the crack tip asymptotic function $\sqrt{r}\sin(\theta/2)$ in reproducing the crack face discontinuity in isotropic materials is demonstrated in Fig. 5. The same notion is also true for orthotropic enrichment functions.

3.6. Transition of displacement and temperature fields between knot spans

Due to the fact that the types of the approximation fields differ in an enriched domain and its neighboring non-enriched domains, a sharp transition between these domains may result in substantial numerical inaccuracies. To avoid this shortcoming, blending elements have been proposed for the case of XFEM, which can be similarly extended to XIGA. In this work, however, another approach has been adopted.

To consider the blending effect and to avoid displacement field discontinuity between the aforementioned selected domain and its neighboring elements/knot spans, all basis functions of elements/knot spans located in the support domain of the enriched nodes/control points (basis function pertaining to elements/knot spans nearby the tip element/knot span, shown by a dark blue domain (in web version) for a particular control point in Fig. 4) are also enriched. This lemma has almost the same smoothing effect as blending elements. It is noted that the Heaviside function does not alter the order of standard IGA basis functions, and therefore, the adopted technique can still be effectively used for the case of transition between a subdomain with the Heaviside enrichment and a subdomain with the crack tip enrichment.

It should be mentioned that while additional smoothness, particularly in the stress field, can be achieved with more advanced transition methods, the adopted technique remains sufficiently

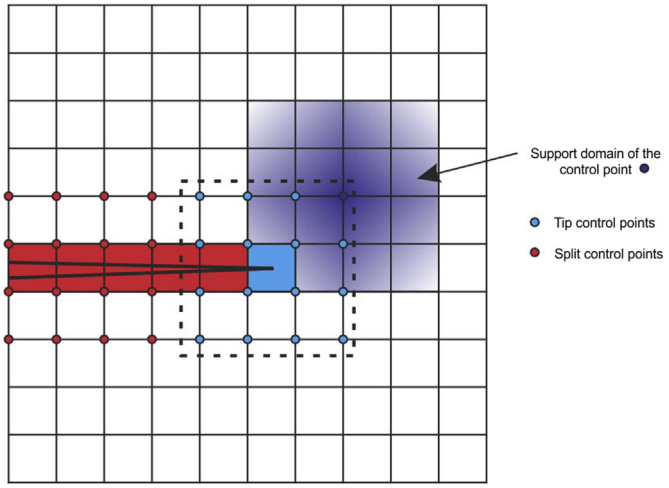

Fig. 4. Definition of different points in XIGA crack modeling.

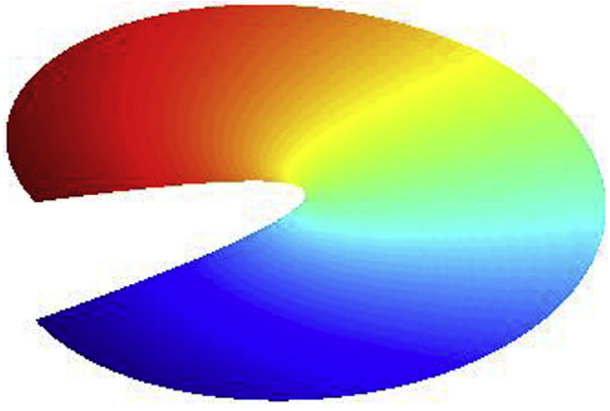

Fig. 5. Crack face displacement discontinuity reproduced by the crack tip enrichment function $\sqrt{r}\sin(\theta/2)$.

accurate when the path independent integral is employed to derive the stress intensity factors. The reason can be attributed to the fact that only field variables which are not in the close vicinity of the crack tip are used for evaluation of SIFs through a domain interaction integral.

3.7. Numerical integration of enriched knot spans

Since the accuracy of Gauss quadrature integration rule significantly decreases in discontinuous domains, the well-developed sub-triangulation technique (Ghorashi et al., 2012) is adopted here. Knot spans containing a crack face or a crack tip are divided into subdomains of sub-triangles, and the Gauss quadrature rule is applied for each of these triangles. The three-stage mapping required in the aforementioned integration technique is presented in Fig. 6. In the last mapping, which is an additional step to the two-stage typical mapping procedure of IGA, the position of crack tip in the parent domain is determined using the Newton–Raphson algorithm. Also For knot spans containing the crack face, the same nonlinear solver is used to obtain the coordinate of any other physical point in the parent domain.

3.8. Stress intensity factor

In this work, the interaction integral method has been used to compute the stress intensity factors. For inhomogeneous problems three formulations of non-equilibrium, incompatibility, and constant–constitutive have been proposed. Non-equilibrium and incompatibility methods lead to more or less similar results, while the constant–constitutive approach is usually less accurate (Kim and Paulino, 2005). Here, only the incompatibility formulation is adopted, in which the auxiliary strain field is calculated from $\varepsilon_{kl}^{\text{aux}} = c_{ijkl}^{-1}(x)\sigma_{ij}^{\text{aux}}$, which results in a different value obtained from $c_{ijkl}^{-1}(x^{\text{tip}})\sigma_{ij}^{\text{aux}} = \frac{1}{2}(u_{i,j}^{\text{aux}} + u_{j,i}^{\text{aux}})$(where x^{tip} is the crack tip coordinate). This discrepancy results in the following incompatible relations:

$$\sigma_{ij,j}^{\text{aux}} = 0, \text{ and } \sigma_{ij}^{\text{aux}} = c_{ijkl}(x)\varepsilon_{kl}^{\text{aux}}, \text{ but } \varepsilon_{ij}^{\text{aux}} \neq \frac{1}{2}\left(u_{i,j}^{\text{aux}} + u_{j,i}^{\text{aux}}\right) \quad (38)$$

where superscript *aux* denotes the auxiliary fields. Now, back to the definition of the equivalent domain integral form of the J-integral for a cracked body:

$$J = \int_A (\sigma_{ij}u_{i,1} - w\delta_{1j})q_{,j}dA + \int_A (\sigma_{ij}u_{i,1} - w\delta_{1j})_{,j}qdA \quad (39)$$

where δ_{ij} is the Kronecker delta and w is the strain energy density,

$$w = \frac{1}{2}(\sigma_{11}\varepsilon_{11}^{\text{m}} + \sigma_{22}\varepsilon_{22}^{\text{m}} + 2\sigma_{12}\varepsilon_{12}^{\text{m}}) \quad (40)$$

in plane stress condition. A is the interior region of the arbitrary contour Γ surrounding the crack tip (Fig. 7), and q is a smooth function ranging from $q = 1$ on the interior boundary of surface A to $q = 0$ on the outer one, as depicted in Fig. 7. In thermo-mechanical problems, the interior radius of surface A in Fig. 7 must reduce to zero; so A is an arbitrary region including the crack tip with $q = 1$ at the crack tip and $q = 0$ on the outer boundary of A.

Using the conservation J integral for two acceptable auxiliary and actual states, the interaction integral method is employed in this paper to calculate the mixed mode stress intensity factors

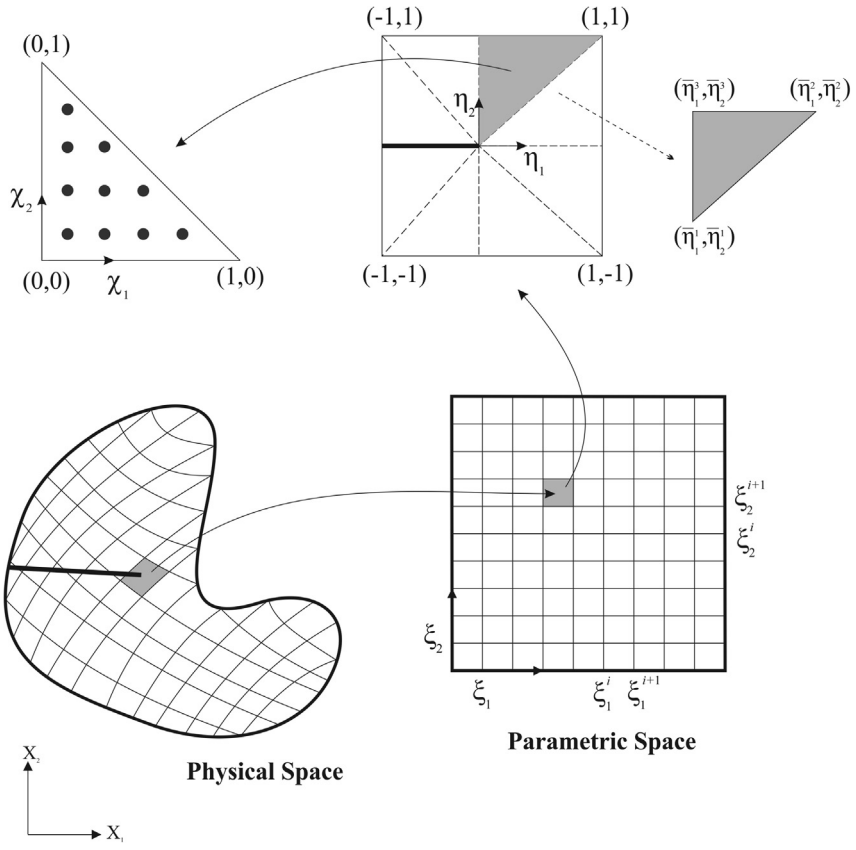

Fig. 6. Different mappings used in the integration over enriched elements.

$$J = J^{act} + J^{aux} + M \tag{41}$$

where J^{act}, and J^{aux} are the conservation integrals corresponding to actual and auxiliary fields, respectively. Since no analytical solution is available in the literature for FGM solids, the acceptable auxiliary stress and displacement fields used in this study are those derived at a crack tip for a homogenous orthotropic body (see Appendix B). M denotes the interaction integral and consists of mechanical and thermal terms for a thermo-mechanical problem (Hosseini et al., 2013)

$$M = M^{m} + M^{th} \tag{42}$$

with

$$M^{m} = \int_A \left\{ \sigma_{ij} u^{aux}_{i,1} + \sigma^{aux}_{ij} u_{i,1} - \frac{1}{2}\left(\sigma_{ik}\varepsilon^{aux}_{ik} + \sigma^{aux}_{ik}\varepsilon^{m}_{ik}\right)\delta_{1j} \right\} q_{,j} dA + \int_A \left\{ \sigma_{ij}\left(s^{tip}_{ijkl} - s_{ijkl}(x)\right)\sigma^{aux}_{kl,1} \right\} q dA \tag{43}$$

$$M^{th} = \int_A \left\{ \sigma^{aux}_{ij} \varepsilon^{th}_{ij,1} \right\} q dA = \int_A \left\{ \sigma^{aux}_{ii} \left[\lambda_{ii,1}(\Delta T) + \lambda_{ii} T_{,1} \right] \right\} q dA \tag{44}$$

where λ_{ij} is related to the thermal expansion coefficient α_{ij},

$$\lambda_{11} = \alpha_{11}; \quad \lambda_{22} = \alpha_{22}; \quad \lambda_{33} = \alpha_{33}; \quad \lambda_{12} = 0 \tag{45}$$

for the plane stress state. For plane strain problems, the following amendments to Eq. (45) are required,

$$\lambda_{11} = \nu_{31}\alpha_{33} + \alpha_{11}; \quad \lambda_{22} = \nu_{32}\alpha_{33} + \alpha_{22}; \quad \lambda_{33} = \alpha_{33}; \quad \lambda_{12} = 0 \tag{46}$$

where ν_{ij} denotes Poison's ratio. In addition, further modification to Eq. (40) is required to account for ε^{m}_{33}(Jirasek and Belytschko, 2002). It is also worth mentioning that the thermal effects are negligible in the auxiliary state and $\boldsymbol{\varepsilon}^{aux}$ can be reduced to contain only the mechanical strain.

The interaction integral M is related to the stress intensity factors with the following equation (Kim and Amit, 2008)

$$M = 2c_{11}K^{aux}_{I}K_{I} + c_{12}\left(K^{aux}_{I}K_{II} + K^{aux}_{II}K_{I}\right) + 2c_{22}K^{aux}_{II}K_{II} \tag{47}$$

with

$$c_{11} = -\frac{a_{22}}{2} Im\left(\frac{\mu_1 + \mu_2}{\mu_1\mu_2}\right) \tag{48}$$

$$c_{12} = -\frac{a_{22}}{2} Im\left(\frac{1}{\mu_1\mu_2}\right) + \frac{a_{11}}{2} Im(\mu_1\mu_2) \tag{49}$$

$$c_{22} = \frac{a_{11}}{2} Im(\mu_1 + \mu_2) \tag{50}$$

where μ_i are the roots of characteristic Eq. (35).

The mode I and II stress intensity factors can be evaluated by solving the two simple simultaneous equations

$$\begin{cases} M^{l}_{1} = 2c_{11}K_{I} + c_{12}K_{II} & (K^{aux}_{I} = 1 \text{ and } K^{aux}_{II} = 0) \\ M^{l}_{2} = c_{12}K_{I} + 2c_{22}K_{II} & (K^{aux}_{I} = 0 \text{ and } K^{aux}_{II} = 1) \end{cases} \tag{51}$$

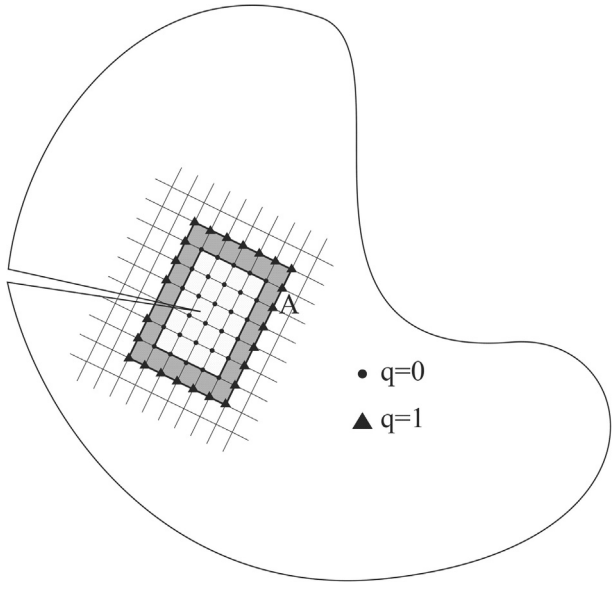

Fig. 7. Equivalent domain form of the J-integral.

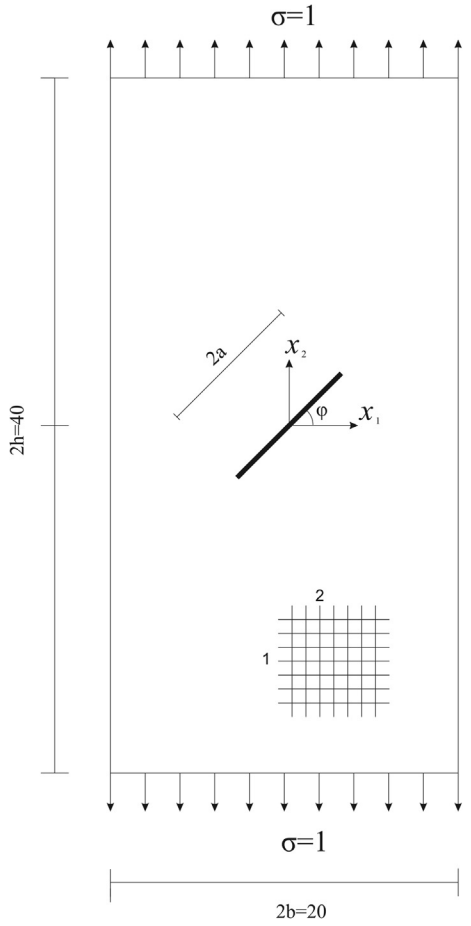

Fig. 8. The orthotropic finite plate containing an oblique crack.

4. Numerical examples

4.1. Central slanted crack in an orthotropic plate

The first example is dedicated to a classical problem of mixed mode fracture of a homogenous rectangular tensile orthotropic plate with a central 45° slanted crack of length $2a = 2$ (Fig. 8). A constant tensile traction ($\sigma = 1$) is applied and the orthotropic material properties are assumed to be

$$E_{11} = 3.5^{\text{GPa}}, \quad E_{22} = 12^{\text{GPa}}, \quad G_{12} = 3^{\text{GPa}}, \quad \nu_{21} = 0.7$$

Several authors have solved this problem and evaluated the mixed-mode stress intensity factors by using different analytical and numerical techniques: Sih et al. (1965), Alturi et al. (1975), Wang et al. (1980), Kim and Paulino (2002), and finally Asadpoure et al. (2006a) and Asadpoure and Mohammadi (2007) (XFEM combined with the interaction integral method). The XFEM model included 5064 degrees of freedom with a much more dense mesh in the vicinity of the crack. In XIGA, however, the SIF values are calculated by total 3364 degrees of freedom with a uniform mesh (55 × 55 knot spans) and quadratic splines in both directions. Moreover, the analysis is performed by utilizing the orthotropic enrichment functions and the M-integral method (Section 3.6) with the relative integration domain size of 0.8. The reference and obtained results are compared in Table 1.

To further asses the credibility of the proposed approach, values of stress intensity factors for different crack angles are calculated by XIGA and compared with those obtained by XFEM (Asadpoure et al., 2006a) in Fig. 9, which shows a close agreement.

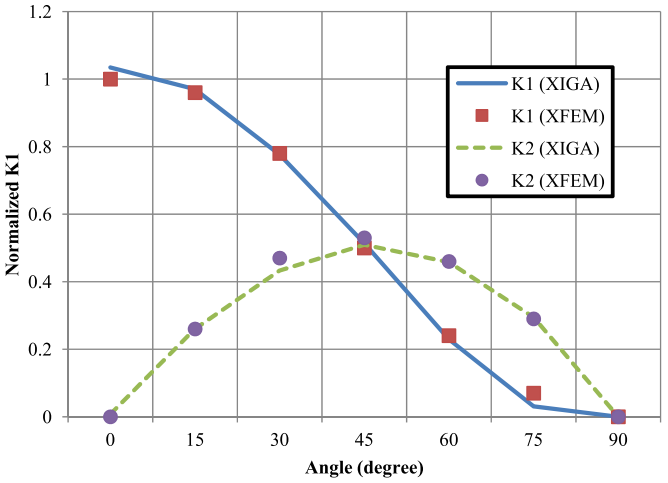

Fig. 9. Comparison of the results obtained by XIGA and XFEM.

4.2. Arc-shaped specimen

To further examine the proposed approach for a more complicated geometry, a crack in an arc-shaped specimen is considered (Fig. 10). The NURBS elements, control points, and the associated weights used for constructing the semicircles are presented in Fig. 11. Linear and cubic splines with associated knot vectors are used to construct the geometry:

$$\Xi = \{0, 0, 0, 0, 1, 1, 1, 1\}$$

$$\Theta = \{0, 0, 1, 1\}$$

Material properties and geometric descriptions are

$$E = 1000 \text{ GPa}, \quad \upsilon = .3$$

$$\frac{X}{W} = 1, \; R = 2$$

The problem is solved by 30 × 30 knot spans in the plane stress state. The stress intensity factors are calculated by a domain integral of radius $r = 0.2$, and the results are compared in Fig. 12 with those reported in (Tada et al., 2000) based on the boundary collocation method. Clearly, very good agreements exist between the results.

Table 1
Comparison of SIFs for the present and reference results.

Method	K_I	$\overline{K}_I$	K_{II}	$\overline{K}_{II}$
XFEM (Asadpoure et al., 2006a)	1.081	0.513	1.092	0.518
XFEM (Asadpoure and Mohammadi, 2007)	1.084	0.514	1.095	0.519
Sih et al. (1965)	1.054	0.500	1.054	0.5
Alturi et al. (1975)	1.019	0.484	1.079	0.512
Wang et al. (1980)	1.023	0.485	1.049	0.498
Kim and Paulino (2002)	1.077	0.511	1.035	0.495
XIGA (Present method)	1.083	0.514	1.074	0.509

4.3. Square plate with a center crack under thermal loading

In this example, for the first time, a thermal fracture problem is solved by XIGA. A center crack in a homogenous isotropic square plate containing an adiabatic crack, with a heat flux perpendicular to the crack surface, in plane strain state is considered, as illustrated in Fig. 13. The temperature of ± 1000° is applied at the top and bottom edges, and the left and right edges and the crack faces are assumed to be insulated. Different crack lengths are analyzed in this study. The details are

$$L = 1, \quad \alpha = 1.67 \times 10^{-5}, \quad E = 218.4 \times 10^{9} \text{ Pa}, \quad \upsilon = 0.3$$

The domain is discretized with a uniform mesh consisting of 25 × 25 knot spans, which is far less than the 3632 elements used by reference (Duflot, 2008). In terms of the order of splines, quadratic functions are used in both parametric directions. The stress intensity factors are calculated with a relative integration domain size of 0.3 and are compared with those reported by Murakami (1987), Prasad et al. (1994b) (BEM), and Duflot (2008) (XFEM) in Table 2. The results are normalized by $2\alpha\theta E\sqrt{L}$, with α being the expansion coefficient.

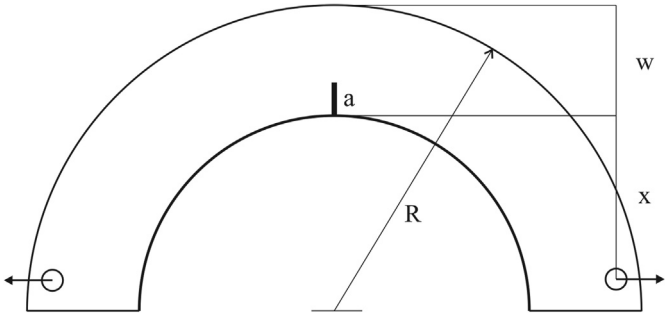

Fig. 10. Arc-shaped specimen.

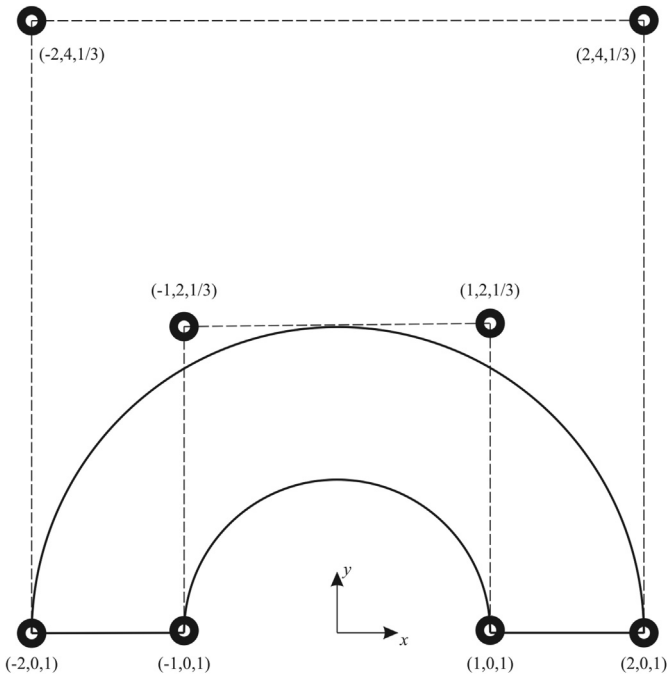

Fig. 11. Scaffold of control points defining the cubic circle.

By enriching the temperature field in XIGA, both the discontinuity in the temperature and the singularity in the heat flux around the crack tips are reproduced, as illustrated in Figs. 14 and 15, respectively.

In order to show the insensitivity of stress intensity factors to the selection of J-integral domain, Fig. 16 depicts the values of K/K_{exact} computed from different J-integral domain radii. Clearly, the stress intensity factors remain constant for different radii of contour integral.

Table 3 illustrates the effect of tip enrichment. Solutions without the tip enrichment, even in very fine meshes are extremely inaccurate. However, by using the tip enrichments, all SIFs, even with the very coarse mesh, are within 2% of the reference values.

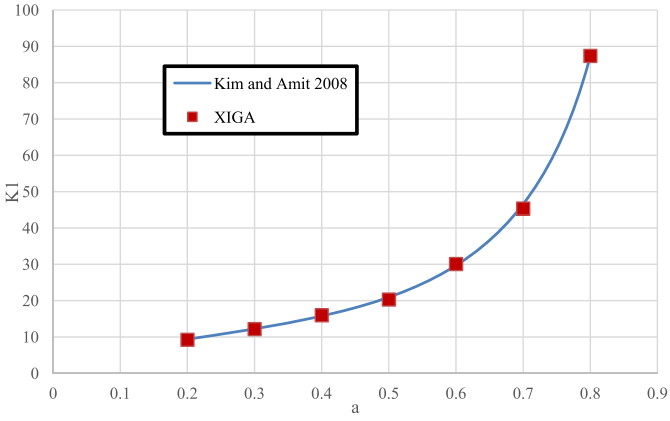

Fig. 12. Comparison of the results obtained by XIGA and the reference boundary collocation method.

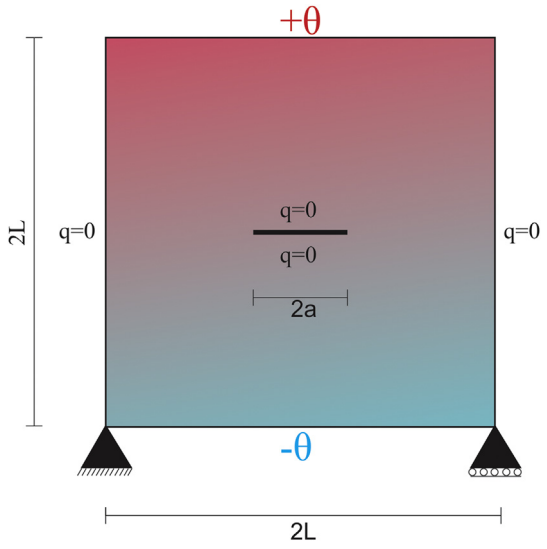

Fig. 13. Pure mode-II adiabatic crack problem.

4.4. Rectangular plate with an inclined crack under thermal loading

To further examine the performance of the proposed XIGA in thermal mixed-mode conditions, an inclined adiabatic crack and with different crack lengths and angles is analyzed. The geometry is depicted in Fig. 17 and the thermal boundary conditions and material properties are similar to the previous example. The dimensions are

$$L/W = 0.5$$

Values of stress intensity factors for various crack lengths and angles are presented in Tables 4 and 5. The results are normalized by $\alpha\theta(W/L)E\sqrt{2W}$, with α being the expansion coefficient. The problem is solved by 35 × 35 knot spans (1444 degrees of freedom), quadratic NURBS basis functions and 4 × 4 gauss quadrature integration rule. As the crack angle increases, the mode I SIF increases, gradually reaches to its maximum at 45°, and then decreases to vanish at 90°. The mode II SIF, however, constantly decreases, as expected from the nature of the problem (note that the crack in 90° configuration becomes parallel to the heat flux). Figs. 18 and 19 illustrate the temperature field and heat flux distribution for the crack length $a = 0.4$ and crack angle45°.

To investigate the effect of different Gauss quadrature rules and different NURBS orders on the accuracy, relative errors in mode-II stress intensity factor for the case of crack angle 0° are presented in Fig. 20. As expected, the results for different gauss points become constant after a specific number. The level of error remains almost the same for different NURBS orders, with a slightly more accurate prediction by the second order NURBS.

Table 2
Values of normalized mode-II stress intensity factors.

Half crack length a	Ref (Murakami, 1987)	Ref (Prasad et al., 1994b)	Ref (Duflot, 2008)	XIGA
0.3	0.094	0.095	0.096	0.094
0.4	0.141	0.141	0.141	0.141
0.5	0.188	0.190	0.191	0.187
0.6	0.247	0.243	0.245	0.242

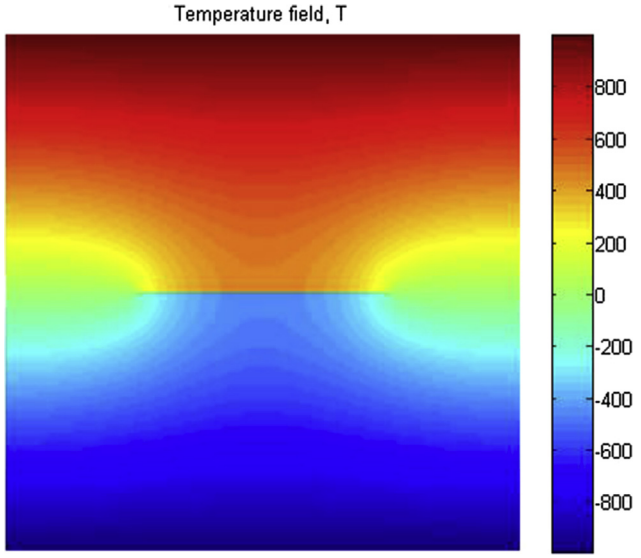

Fig. 14. Variations of temperature field (°C) for the crack length $a = 0.5$.

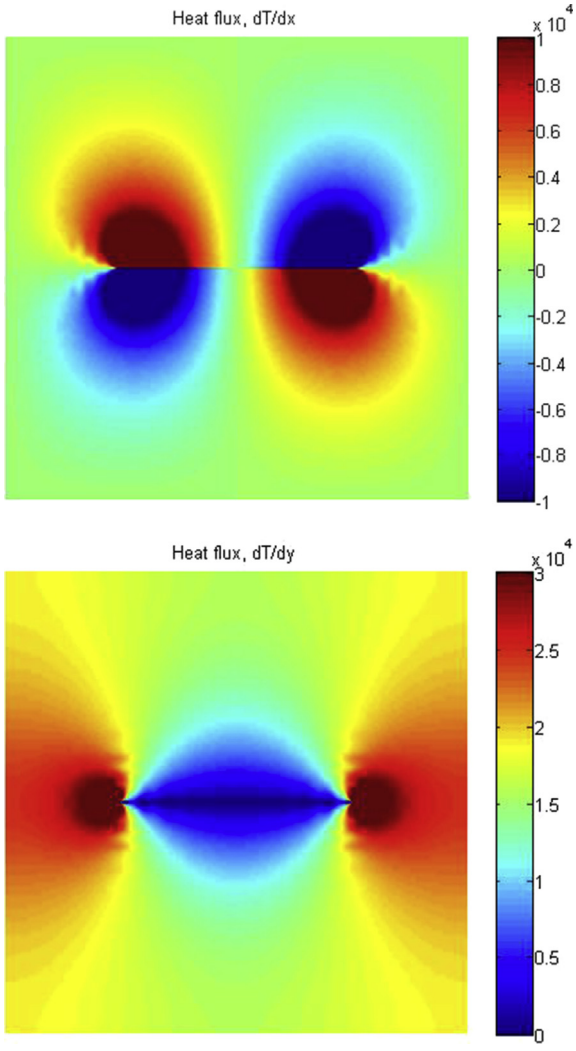

Fig. 15. Contours of heat flux (°C/mm) for the crack length $a = 0.5$.

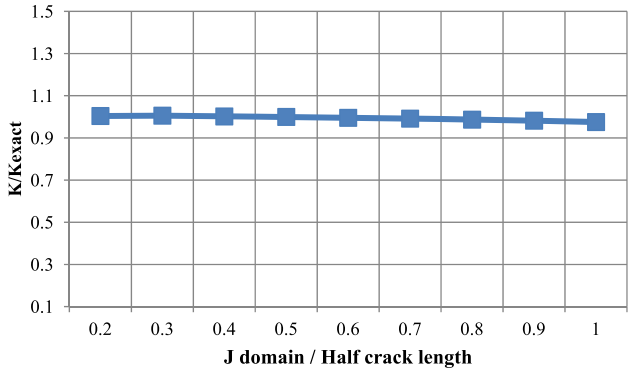

Fig. 16. Path-dependent J-integral.

Also, Fig. 21 provides values of J/J_{exact} versus various crack lengths, clearly indicating the indifference of the J-integral value with respect to the radius of contour integral. In isotropic materials and for plane strain states, the exact value of J-integral can be obtained from the SIF by the following relation

$$J = \frac{K_1^2 + K_2^2}{E}\left(1 - \nu^2\right)$$

4.5. FGM plate with a center crack under mechanical loading

In this example, a cracked inhomogeneous plate under a constant strain loading $\bar{\varepsilon}$ at the top and bottom edges is considered. The constant strain is applied by assigning an equal stress load $\sigma_{22} = E\bar{\varepsilon}$ at the top and bottom edges. The crack is parallel to material gradient and the displacements of the center nodes of the left and right edges are fixed (Fig. 22). Dimensions are

$$L = 10, \quad a = 1$$

Table 3
Effect of tip enrichment for three different knot spans.

Number of knot spans	With enrichment		Without enrichment	
	K_I	Relative error %	K_I	Relative error %
625	0.1399	1.47	0.0820	41.81
3025	0.1401	0.61	0.1120	20.52
7225	0.1404	0.44	0.1216	13.76

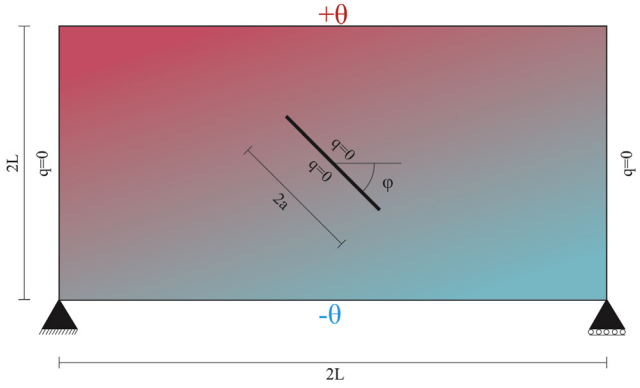

Fig. 17. Mixed mode adiabatic crack problem.

Table 4
Normalized mixed mode stress intensity factors for different crack lengths.

Half crack length	K_I				K_{II}			
	Ref (Murakami, 1987)	Ref (Prasad et al., 1994b)	Ref (Duflot, 2008)	XIGA	Ref (Murakami, 1987)	Ref (Prasad et al., 1994b)	Ref (Duflot, 2008)	XIGA
0.2	0.002	0.002	0.002	0.001	0.030	0.030	0.0302	0.029
0.3	0.008	0.006	0.0068	0.005	0.048	0.048	0.0489	0.046
0.4	0.015	0.014	0.0149	0.012	0.064	0.064	0.0650	0.062
0.5	0.027	0.026	0.0265	0.025	0.076	0.076	0.0774	0.076

Table 5
Normalized mixed mode stress intensity factors for different crack angles.

Crack angle	K_I				K_{II}			
	Ref (Murakami, 1987)	Ref (Prasad et al., 1994b)	Ref (Duflot, 2008)	XIGA	Ref (Murakami, 1987)	Ref (Prasad et al., 1994b)	Ref (Duflot, 2008)	XIGA
0°	0.0000	0.0000	0.0000	0.0001	0.054	0.054	0.0546	0.053
15°	0.0038	0.0036	0.0038	0.0032	0.054	0.054	0.0533	0.051
30°	0.0071	0.0064	0.0068	0.0060	0.048	0.048	0.0489	0.048
45°	0.0077	0.0071	0.0076	0.0068	0.042	0.041	0.0420	0.041
60°	0.0053	0.0049	0.0054	0.0046	0.032	0.032	0.0322	0.030
75°	0.0023	0.0010	0.0017	0.0009	0.018	0.018	0.0180	0.017
90°	0.0000	0.0003	0.0000	0.0000	0.000	0.000	0.0000	0.000

This orthotropic functionally graded plate is assumed to possess exponentially variable Young's and shear modulus, while the Poisson's ratio remains constant.

$$E_{11}(x_1) = E_{11}^0 e^{\beta x_1}, \quad E_{22}(x_1) = E_{22}^0 e^{\beta x_1}, \quad G_{12}(x_1) = G_{12}^0 e^{\beta x_1}$$

In the orthotropic medium, the effective Young's modulus$E$, and the effective Poisson's ratio are defined as

$$E = \sqrt{E_{12}E_{21}}, \quad \upsilon = \sqrt{\upsilon_{12}\upsilon_{21}}$$

95 × 95 knot spans with a total of 9604 degrees of freedom in a uniform mesh, and quadratic splines in both directions are employed for modeling the problem. Table 6 provides the normalized SIF for different inhomogeneity parameters (β) and compares the results with those reported by Kim and Paulino (2003), who used a very fine unstructured mesh with 5851 degrees of freedom near the crack tip. The Normalization factor K_0 is defined as

$$K_0 = \bar{\varepsilon}\bar{E}^0\sqrt{\pi a}, \quad \bar{E}^0 = \frac{E^0}{\delta^2}, \quad E^0 = \sqrt{E_{11}E_{22}}, \quad \delta^4 = \frac{E_{11}}{E_{22}} = \frac{\upsilon_{12}}{\upsilon_{21}}$$

Additionally, the effects of Poisson' ratio on SIF is investigated and compared with Refs. Kim and Paulino (2003), Bayesteh and Mohammadi (2013), Ozturk and Erdogan (1999) in Table 7. Clearly, variation of the effective Poisson's ratio has an insignificant effect on the normalized SIF.

To assess the convergence rate of error of normalized SIF, this example is modeled by six different meshes. Fig. 23 shows that after about 10,000 degrees of freedom, the results become sufficiently accurate. Furthermore, Fig. 24 depicts the insensitivity of the SIF computed from these six meshes with respect to the number of knot spans, confirming that the results are mesh-independent.

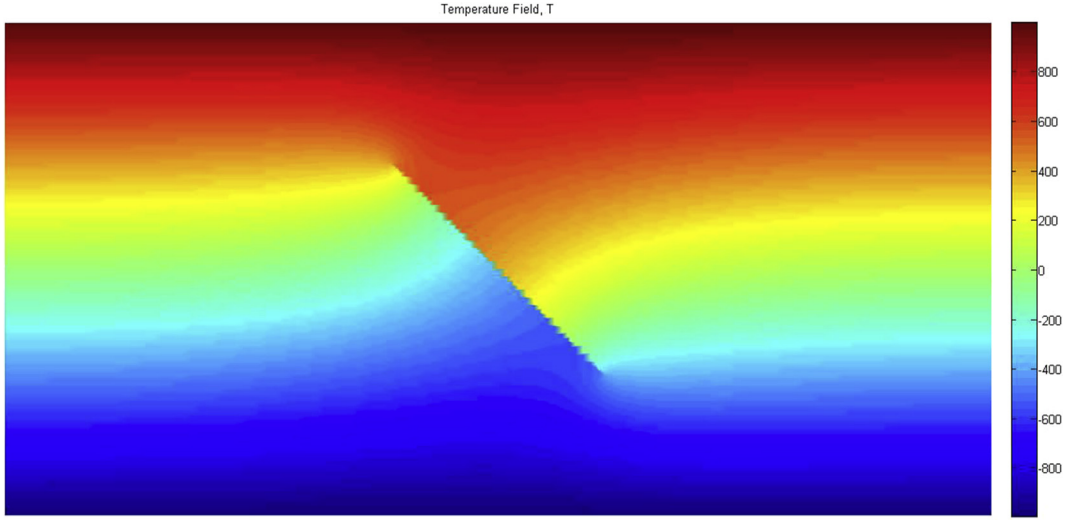

Fig. 18. Contour of the temperature (°C) field.

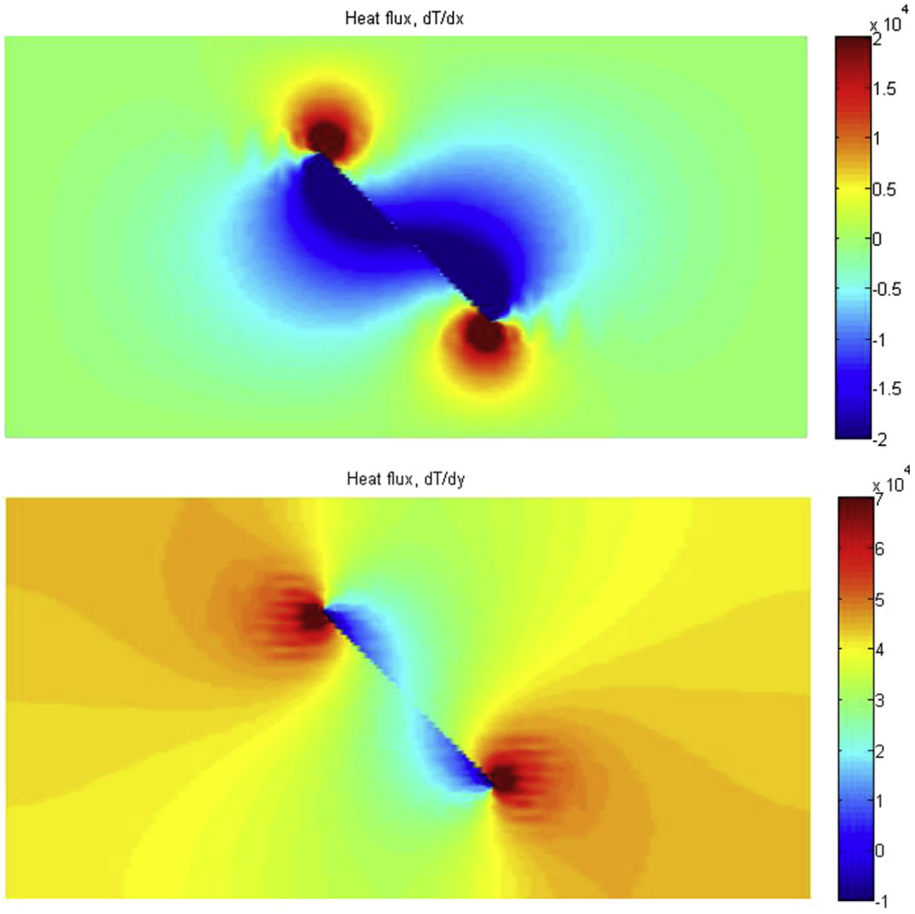

Fig. 19. Variation of the heat flux (°C/mm) in X and Y direction.

To further demonstrate the capability of XIGA, the same FGM is now considered under the thermal loading (Fig. 25). Material and geometric properties are

$$E_{11}(x_1) = E_{11}^0 e^{\beta x_1}; \quad E_{22}(x_1) = E_{22}^0 e^{\beta x_1}; \quad G_{12}(x_1) = G_{12}^0 e^{\beta x_1}$$
$$\alpha_{11}(x_1) = \alpha_{11}^0 e^{\beta x_1}; \quad \alpha_{22}(x_1) = \alpha_{22}^0 e^{\beta x_1}$$
$$E_{11}^0 = 10^4; \quad E_{22}^0 = 10^3; \quad G_{12}^0 = 1216; \quad \upsilon_{12} = 0.3$$
$$L = 10, \quad a = 1$$

The prescribed temperature field $\Delta\theta = e^{-\beta x_1}/\alpha_{ii}$ is applied to the plate to trigger the crack. The problem is solved by 105 × 105 knot spans in the plane stress state and the stress intensity factor (normalized by the $K_0 = E_{22}^0\sqrt{\pi a}$) for different cases of inhomogeneity parameter β is depicted in Fig. 26, which shows the increase of SIF with the increase of β. Also, in $\beta = 0.5$ the result is compared with the reference value (Kim and Amit, 2008).

4.6. Cracked plate with a central hole

This example consists of four cracks emanating from a hole in a rectangular tensile plate (Fig. 27). This example is provided to show the capability of XIGA to handle fracture analysis of complex

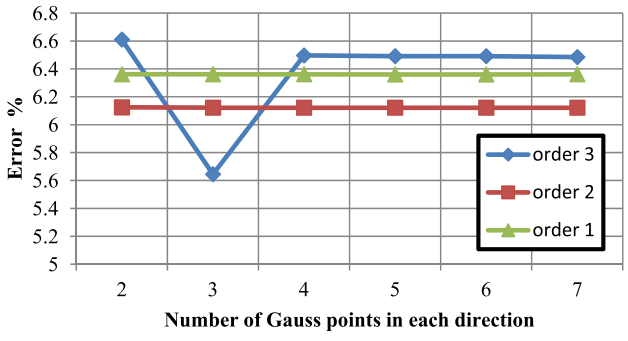

Fig. 20. Effect of Gauss quadrature rules and NURBS polynomial order on the accuracy of K_{II}.

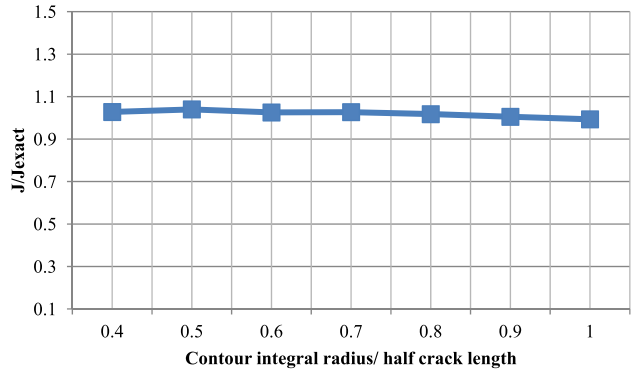

Fig. 21. J-Integral value for different contour integral radii.

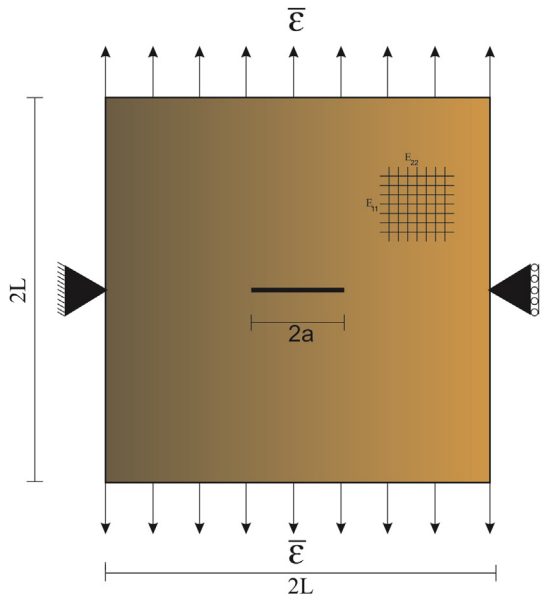

Fig. 22. Geometry and mechanical properties of the FGM plate.

geometries. The dimensions and material properties of this plane stress problem are

$$b = 4, \quad h = 8, \quad R = 1, \quad a = 1.4$$

$$E = 1000e^{\beta y}$$

$$\nu = 0.3$$

Considering the symmetry, the original geometry of the problem is constructed by using 18 control points (Fig. 28 and Table 8). 25×25 knot spans are used and the results of normalized stress intensity factors are provided in Table 9 for both crack tips as the crack angle changes in the case of $\beta = 0.5$(results are normalized by$\sigma\sqrt{\pi a}$). Note that variable material properties cause dissimilar values for upper and lower cracks. Also, Fig. 29 depicts the SIFs obtained from different contour integrals for the case of $\overline{\alpha} = 45^\circ$ and $\beta = 0.3$, showing that the J-integral is practically path independent.

Table 6
Comparison of the stress intensity factors.

β_a	0	0.1	0.25	0.5	0.75	1
Ref (Kim and Paulino, 2003)	0.9969	1.0750	1.2043	1.4371	1.7055	2.0318
XIGA	1.0052	1.0769	1.2069	1.4358	1.7121	2.0237

Table 7
The effect of Poisson's ratio.

υ	K_I/K_0			
	Ref (Bayesteh and Mohammadi, 2013)	Ref (Kim and Paulino, 2003)	Ref (Ozturk and Erdogan, 1999)	Present XIGA
0.1	1.3996	1.4300	1.4183	1.4188
0.2	1.4398	1.4334	1.4223	1.4292
0.3	1.4381	1.4371	1.4280	1.4357
0.4	1.4475	1.4405	1.4325	1.4392
0.5	1.4435	1.4438	1.4368	1.4441
0.7	1.4581	1.4505	1.4449	1.4467
0.9	1.4568	1.4563	1.4524	1.4512

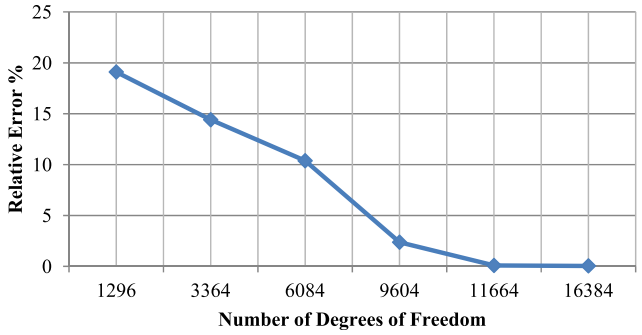

Fig. 23. Variation of the relative error with respect to the number of degrees of freedom.

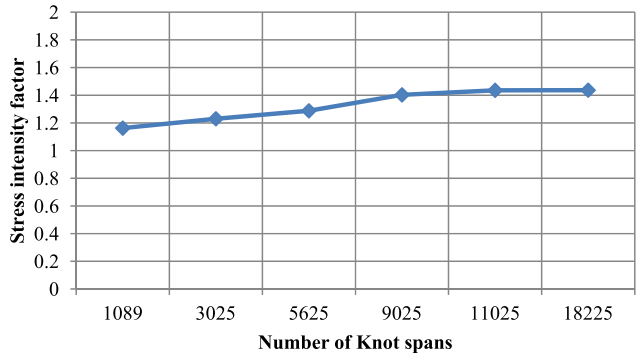

Fig. 24. Sensitivity of the results, with respect to the number of knot spans.

The knot vectors are

$$\Xi = \{0, 0, 0, .25, .25, .5, .5, .75, .75, 1, 1, 1\}$$

$$\Theta = \{0, 0, 1, 1\}$$

Table 10 depicts the calculated normalized stress intensity factors for different values of the inhomogeneity parameter β for the

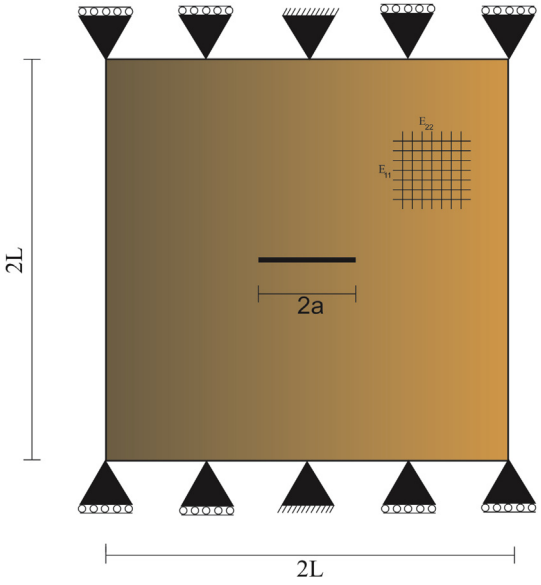

Fig. 25. FGM-plate under thermal loading.

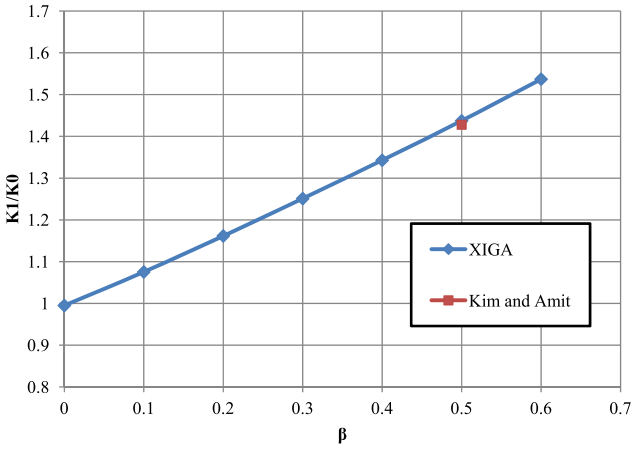

Fig. 26. Variations of the stress intensity factor with respect to β.

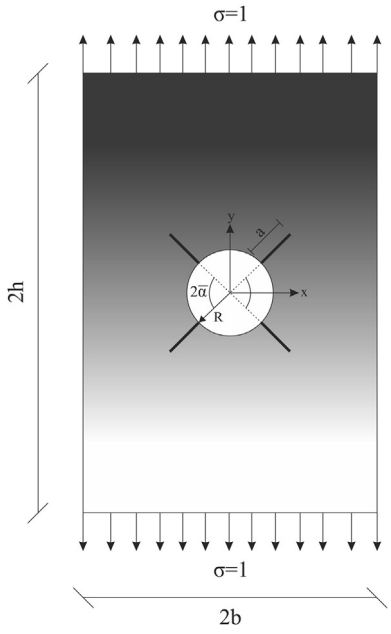

Fig. 27. Tensile FGM plate with cracks emanating from a central hole.

case of $\bar{\alpha} = 45^{\circ}$. Clearly, as the material becomes more inhomogeneous, the stress intensity factors of upper crack increases while for the lower crack the stress intensity factors show a decreasing trend.

5. Conclusion

Fracture of functionally graded materials under thermal loadings has been analyzed by the extended isogeometric analysis. Enrichment functions are added to the original displacement field to model crack face displacement discontinuity and crack tip stress singularity. Mixed mode stress intensity factors, obtained from the interaction integral, are in close agreement with the reference results. Hence, XIGA can be used as an alternative for fracture analysis of problems involving crack solids under thermal loading, particularly problems in which constructing the geometry and approximating the solution with the same functions is an advantage for the analyst.

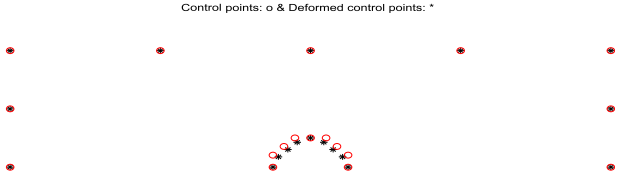

Fig. 28. Representation of the problem geometry by 18 control points.

Table 8
Control points and their associated weights.

Control point	x	y	Weight
1	−1	0	1
2	−0.8536	0.3536	0.8536
3	−0.06036	0.6036	0.8536
4	−0.3536	0.8536	0.8536
5	0	1	1
6	0.3536	0.8536	0.8536
7	0.6036	0.6036	0.8536
8	0.8536	0.3536	0.8536
9	1	0	1
10	−8	0	1
11	−8	2	1
12	−8	4	1
13	−4	4	1
14	0	4	1
15	4	4	1
16	8	4	1
17	8	2	1
18	8	0	1

Table 9
Variation of normalized stress intensity factors as a function of center angle.

$\bar{\alpha}$	Upper crack		Lower crack	
	K_I	K_{II}	K_I	K_{II}
30°	0.732	0.473	1.354	0.391
45°	0.486	0.551	0.790	0.650
60°	0.144	0.435	0.355	0.591

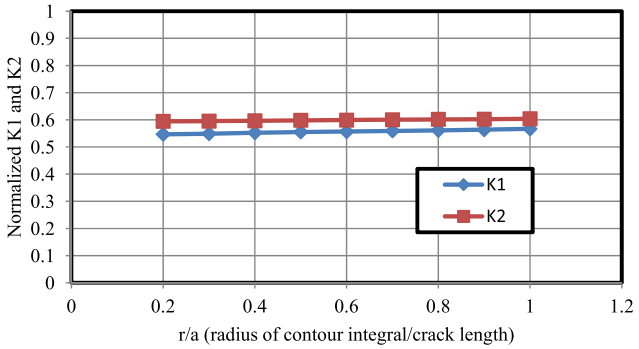

Fig. 29. Path independent J-integral.

Table 10
Variation of normalized stress intensity factors as a function of β.

β	Upper crack		Lower crack	
	K_I	K_{II}	K_I	K_{II}
0	0.927	0.834	0.927	0.834
0.1	0.906	0.824	0.949	0.846
0.2	0.880	0.808	0.974	0.859
0.3	0.852	0.791	1.001	0.871
0.4	0.820	0.771	1.025	0.878
0.5	0.786	0.751	1.049	0.882

Acknowledgment

The authors would like to acknowledge the financial support of University of Tehran for this research under the Grant no. 8102051/1/005. Also, the technical support of the High Performance Computing Lab, School of Civil Engineering, University of Tehran is appreciated. Furthermore, the financial support of Iran National Science Foundation (INSF) is gratefully acknowledged.

Appendix A

Components of the extended stiffness matrix and the force vector, in the mechanical loading, are (Mohammadi, 2008)

$$\mathbf{K}^{rs} = \int_{\Omega^e} (\mathbf{B}^r)^T \mathbf{D}\mathbf{B}^s \mathrm{d}\Omega \quad (r,s = u,a,b) \tag{A1}$$

$$\mathbf{f}_i^u = \int_{\Gamma_t} N_i \mathbf{f}^t \mathrm{d}\Gamma + \int_{\Omega^e} N_i \mathbf{f}^b \mathrm{d}\Gamma \tag{A2}$$

$$\mathbf{f}_i^a = \int_{\Gamma_t} N_i H \mathbf{f}^t \mathrm{d}\Gamma + \int_{\Omega^e} N_i H \mathbf{f}^b \mathrm{d}\Gamma \tag{A3}$$

$$\mathbf{f}_i^{b_\alpha} = \int_{\Gamma_t} N_i F_\alpha \mathbf{f}^t \mathrm{d}\Gamma + \int_{\Omega^e} N_i F_\alpha \mathbf{f}^b \mathrm{d}\Gamma \quad (\alpha = 1,2,3, \text{ and } 4) \tag{A4}$$

where $\mathbf{f}^t$ is the external traction force, $\mathbf{f}^b$ is the body force, $\mathbf{D}$ is the elasticity matrix, N_i are NURBS basis functions, and $\mathbf{B}^r$ are matrices of basis functions derivatives,

$$\mathbf{B}_i^u = \begin{bmatrix} N_{i,x} & 0 \\ 0 & N_{i,y} \\ N_{i,y} & N_{i,x} \end{bmatrix} \tag{A5}$$

$$\mathbf{B}_i^a = \begin{bmatrix} (N_i H)_{,x} & 0 \\ 0 & (N_i H)_{,y} \\ (N_i H)_{,y} & (N_i H)_{,x} \end{bmatrix} \tag{A6}$$

$$\mathbf{B}_i^b = [\, \mathbf{B}_i^{b_1} \quad \mathbf{B}_i^{b_2} \quad \mathbf{B}_i^{b_3} \quad \mathbf{B}_i^{b_4} \,] \tag{A7}$$

$$\mathbf{B}_i^{b_\alpha} = \begin{bmatrix} (N_i F_\alpha)_{,x} & 0 \\ 0 & (N_i F_\alpha)_{,y} \\ (N_i F_\alpha)_{,y} & (N_i F_\alpha)_{,x} \end{bmatrix} \quad (\alpha = 1,2,3, \text{ and } 4) \tag{A8}$$

where F_α and H are the tip and Heaviside enrichment functions.

In the thermal loading condition, the components of the extended stiffness matrix and the force vector are defined as

$$\mathbf{Q}^{rs} = \int_{\Omega^e} (\mathbf{B}^{th-r})^T \kappa \mathbf{B}^{th-s} \mathrm{d}\Omega \quad (r,s = \mathrm{u},\mathrm{a},\mathrm{b}) \tag{A9}$$

$$\mathbf{f}^{\mathrm{th}-u} = \int_{\Gamma_q} N_i \, \bar{q} \, d\Gamma \tag{A10}$$

$$\mathbf{f}_i^{\mathrm{th}-a} = \int_{\Gamma_t} N_i H \bar{q} \mathrm{d}\Gamma \tag{A11}$$

$$\mathbf{f}_i^{th-b_1} = \int_{\Gamma_t} N_i F_\alpha \bar{q} \mathrm{d}\Gamma \tag{A12}$$

Here, the matrices of basis functions derivatives are defined as

$$\mathbf{B}_i^{\mathrm{th}-\mathrm{u}} = \begin{bmatrix} N_{i,x} \\ N_{i,y} \end{bmatrix} \tag{A13}$$

$$\mathbf{B}_i^{\mathrm{th}-\mathrm{a}} = \begin{bmatrix} (N_i H)_{,x} \\ (N_i H)_{,y} \end{bmatrix} \tag{A14}$$

$$\mathbf{B}_i^{\mathrm{th}-\mathrm{b}_1} = \begin{bmatrix} (N_i F_{th})_{,x} \\ (N_i F_{th})_{,y} \end{bmatrix} \tag{A15}$$

and

$$\kappa = \begin{bmatrix} k_{11} & 0 \\ 0 & k_{22} \end{bmatrix} \tag{A16}$$

where F_{th} is the thermal tip enrichment function, and k_{ii} is heat conductivity coefficient in i^{th} direction.

Appendix B

The asymptotic crack-tip displacement fields for a homogenous orthotropic cracked body, as proposed by Bayesteh and Mohammadi (2013), are defined as,

$$u_1^{aux} = K_I \sqrt{\frac{2r}{\pi}} \mathrm{Re}\left\{ \frac{1}{\mu_1^{tip} - \mu_2^{tip}} \left[\mu_1^{tip} p_2^{tip} g_2^{tip}(\theta) - \mu_2^{tip} p_1^{tip} g_1^{tip}(\theta) \right] \right\} + K_{II} \sqrt{\frac{2r}{\pi}} \mathrm{Re}\left\{ \frac{1}{\mu_1^{tip} - \mu_2^{tip}} \left[p_2^{tip} g_2^{tip}(\theta) - p_1^{tip} g_1^{tip}(\theta) \right] \right\} \tag{B1}$$

$$u_2^{aux} = K_I \sqrt{\frac{2r}{\pi}} \mathrm{Re}\left\{ \frac{1}{\mu_1^{tip} - \mu_2^{tip}} \left[\mu_1^{tip} q_2^{tip} g_2^{tip}(\theta) - \mu_2^{tip} q_1^{tip} g_1^{tip}(\theta) \right] \right\} + K_{II} \sqrt{\frac{2r}{\pi}} \mathrm{Re}\left\{ \frac{1}{\mu_1^{tip} - \mu_2^{tip}} \left[q_2^{tip} g_2^{tip}(\theta) - q_1^{tip} g_1^{tip}(\theta) \right] \right\} \tag{B2}$$

and the associated asymptotic crack-tip stress fields are

$$\sigma_{11}^{aux} = \frac{K_I}{\sqrt{2\pi r}} \mathrm{Re}\left\{ \frac{\mu_1^{tip} \mu_2^{tip}}{\mu_1^{tip} - \mu_2^{tip}} \left[\frac{\mu_2^{tip}}{g_2^{tip}(\theta)} - \frac{\mu_1^{tip}}{g_1^{tip}(\theta)} \right] \right\} + \frac{K_{II}}{\sqrt{2\pi r}} \mathrm{Re}\left\{ \frac{1}{\mu_1^{tip} - \mu_2^{tip}} \left[\frac{\left(\mu_2^{tip}\right)^2}{g_2^{tip}(\theta)} - \frac{\left(\mu_1^{tip}\right)^2}{g_1^{tip}(\theta)} \right] \right\} \tag{B3}$$

$$\sigma_{22}^{aux} = \frac{K_I}{\sqrt{2\pi r}} \mathrm{Re}\left\{ \frac{1}{\mu_1^{tip} - \mu_2^{tip}} \left[\frac{\mu_1^{tip}}{g_2^{tip}(\theta)} - \frac{\mu_2^{tip}}{g_1^{tip}(\theta)} \right] \right\} + \frac{K_{II}}{\sqrt{2\pi r}} \mathrm{Re}\left\{ \frac{1}{\mu_1^{tip} - \mu_2^{tip}} \left[\frac{1}{g_2^{tip}(\theta)} - \frac{1}{g_1^{tip}(\theta)} \right] \right\} \tag{B4}$$

$$\sigma_{12}^{aux} = \frac{K_I}{\sqrt{2\pi r}} \mathrm{Re}\left\{ \frac{\mu_1^{tip} \mu_2^{tip}}{\mu_1^{tip} - \mu_2^{tip}} \left[\frac{1}{g_1^{tip}(\theta)} - \frac{1}{g_2^{tip}(\theta)} \right] \right\} + \frac{K_{II}}{\sqrt{2\pi r}} \mathrm{Re}\left\{ \frac{1}{\mu_1^{tip} - \mu_2^{tip}} \left[\frac{\mu_1^{tip}}{g_1^{tip}(\theta)} - \frac{\mu_2^{tip}}{g_2^{tip}(\theta)} \right] \right\} \tag{B5}$$

with

$$g_i^{tip}(\theta) = \sqrt{\cos(\theta) + \mu_i^{tip} \sin(\theta)} \quad (i = 1,2) \tag{B6}$$

$$p_k^{tip} = a_{11}^{tip}\left(\mu_k^{tip}\right)^2 + a_{12}^{tip} - a_{16}^{tip}\mu_k^{tip} \quad (k = 1,2) \tag{B7}$$

$$q_k^{tip} = a_{12}^{tip}\mu_k^{tip} + \frac{a_{22}^{tip}}{\mu_k^{tip}} - a_{26}^{tip} \quad (k = 1,2) \tag{B8}$$

where a_{ij}^{tip} are the material properties at the crack tip (Eq. (19)), μ_k^{tip} are the roots of the characteristic Eq. (38), and (r,θ) are the polar coordinates measured from the crack tip (Fig. 2)

References

Abotula, S., Kidane, A., Chalivendra, V.B., Shukla, A., 2012. Dynamic curving cracks in functionally graded materials under thermo-mechanical loading. Int. J. Solids Struct. 49 (13), 1637–1655.

Alturi, S.N., Kobayashi, A.S., Nakagi, M.A., 1975. Finite element program for fracture mechanics analysis of composite materials. Fract. Mech. Compos. Mater. 86–98.

Asadpoure, A., Mohammadi, S., 2007. Developing new enrichment functions for crack simulation in orthotropic media by the extended finite element method. Int. J. Numer. Methods Eng. 69 (10), 2150–2172.

Asadpoure, A., Mohammadi, S., Vafai, A., 2006. Crack analysis in orthotropic media using the extended finite element method. Thin Walled Struct. 44 (9), 1031–1038.

Asadpoure, A., Mohammadi, S., Vafai, A., 2006. Modeling crack in orthotropic media using a coupled finite element and partition of unity methods. Finite Elem. Anal. Des. 42 (13), 1165–1175.

Ashari, S.E., Mohammadi, S., 2011. Delamination analysis of composites by new orthotropic bimaterial extended finite element method. Int. J. Numer. Methods Eng. 86 (13), 1507–1543.

Ashari, S.E., Mohammadi, S., 2012. Fracture analysis of FRP-reinforced beams by orthotropic XFEM. J. Compos. Mater. 46 (11), 1367–1389.

Bayesteh, H., Mohammadi, S., 2013. XFEM fracture analysis of orthotropic functionally graded materials. Compos. Part B 44, 8–25.

Belytschko, T., Black, T., 1999. Elastic crack growth in finite elements with minimal remeshing. Int. J. Numer. Methods Eng. 45, 601–620.

Belytschko, T., Gracie, R., Ventura, G., 2009. A review of extended/generalized finite element methods for material modeling. Model. Simul. Mater. Sci. Eng. 17 (4).

Benson, D., Bazilevs, Y., Hsu, M., Hughes, T.J.R., 2010. Isogeometric shell analysis. Comput. Methods Appl. Mech. Eng. 199, 276–289.

Benson, D., Bazilevs, Y., Hsu, M., Hughes, T.J.R., 2011. A large deformation, rotation-free, isogeometric shell. Comput. Methods Appl. Mech. Eng. 200, 1367–1378.

Bowie, O., Freese, C.E., 1972. Central crack in plane orthotropic rectangular sheet. Int. J. Fract. 8 (1), 49–58.

Casanova, F., Gallego, A., 2013. NURBS-based analysis of higher-order composite shells. Compos. Struct. 104, 125–133.

Cottrell, J.A., Hughes, T.J.R., Bazilevs, Y., 2009. Isogeometric Analysis: Toward Integration of CAD and FEA. WILEY.

Cox, M.G., 1971. The Numerical Evaluation of B-splines. National Physics Laboratory. DNAC 4.

De Boor, C., 1972. On calculation with B-splines. J. Approx. Theory 6, 50–62.

De Lorenzis, L., Temizer, I., Wriggers, P., Zavarise, G., 2011. A large deformation frictional contact formulation using NURBS-bases isogeometric analysis. Int. J. Numer. Methods Eng. 87 (13), 1278–1300.

De Luycker, E., Benson, D.J., Belytschko, T., Bazilevs, Y., Hsu, M.C., 2011. X-FEM in isogeometric analysis for linear fracture mechanics. Int. J. Numer. Methods Eng. 87 (6), 541–565.

Delale, F., Erdogan, F., 1983. Crack problem for a nonhomogeneous plane. J. Appl. Mech. 50 (3).

Dolbow, J., 1999. An Extended Finite Element Method with Discontinuous Enrichment for Applied Mechanics in Theoretical and Applied Mechanics. Northwestern University, Evanston, IL, USA.

Duflot, M., 2008. The extended finite element method in thermoelastic fracture mechanics. Int. J. Numer. Methods Eng. 74 (5), 827–847.

El-Hadek, M.A., Tippur, H.V., 2003. Dynamic fracture behavior of syntactic epoxy foams: optical measurements using coherent gradient sensing. Opt. Lasers Eng. 40 (4), 353–369.

El-Hadek, M.A., Tippur, H.V., 2003. Dynamic fracture parameters and constraint effects in functionally graded syntactic epoxy foams. Int. J. Solids Struct. 40 (8), 1885–1906.

Erdogan, F., Wu, B.H., 1997. The surface crack problem for a plate with functionally graded properties. J. Appl. Mech. 64 (3), 449–456.

Ghorashi, S.S., Valizadeh, N., Mohammadi, S., 2012. Extended isogeometric analysis for simulation of stationary and propagating cracks. Int. J. Numer. Methods Eng. 89 (9), 1069–1101.

Gu, P., Asaro, R.J., 1997. Cracks in functionally graded materials. Int. J. Solids Struct. 34 (1), 1–17.

Gupta, S., Abotula, S., Chalivendra, V.B., Shukla, A., Chona, R., 2012. Transient thermo-mechanical analysis of dynamic curving cracks in functionally graded materials. Acta Mech. 223 (7), 1485–1506.

Hosseini, S.S., Bayesteh, S., Mohammadi, S., 2013. Thermo-mechanical XFEM crack propagation analysis of functionally graded materials. Mater. Sci. Eng. A 561, 285–302.

Hughes, T.J.R., Cottrell, J.A., Bazilevs, Y., 2005. Isogeometric analysis: CAD, finite elements, NURBS, exact geometry and mesh refinement. Comput. Methods Appl. Mech. Eng. 194, 4135–4195.

Jia, L., 2011. Isogeometric contact analysis: geometric basis and formulation for frictionless contact. Comput. Methods Appl. Mech. Eng. 200, 726–741.

Jin, Z.-H., Paulino, G.H., Dodds Jr., R.H., 2002. Finite element investigation of quasi-static crack growth functionally graded materials using a novel cohesive zone fracture model. J. Appl. Mech. 69 (3), 370–379.

Jirasek, M., Belytschko, T., 2002. Computational resolution of strong discontinuities. In: Mang, H.A., Rammerstorfer, F.G., Eberhardsteiner, J. (Eds.), Fifth World Congress on Computational Mechanics (Vienna, Austria).

Kiendll, J., Bletzinger, K., Linhard, J., Wuchner, R., 2009. Isogeometric shell analysis with Kirchhoff-Love elements. Comput. Methods Appl. Mech. Eng. 198, 3902–3914.

Kim, J.-H., Amit, K.C., 2008. A generalized interaction integral method for the evaluation of the T-stress in orthotropic functionally graded materials under thermal loading. J. Appl. Mech. 75 (5).

Kim, J.-H., Paulino, G.H., 2002. Mixed-mode fracture of orthotropic functionally graded materials using finite elements and modified crack closure method. Eng. Fract. Mech. 69, 1557–1586.

Kim, J.-H., Paulino, G.H., 2003. The interaction integral for fracture of orthotropic functionally graded materials: evaluation of stress intensity factors. Int. J. Solids Struct. 40, 3967–4001.

Kim, J.-H., Paulino, G.H., 2005. Consistent formulation of the interaction integral method for fracture of functionally graded materials. J. Appl. Mech. 72, 351–364.

Konda, N., Erdogan, F., 1994. The mixed mode crack problem in a nonhomogeneous elastic medium. Eng. Fract. Mech. 47 (4), 533–545.

Kuo, M., Bogy, D.B., 1974. Plane solutions for the displacement and traction-displacement problem for anisotropic elastic wedges. J. Appl. Mech. 41, 197–203.

Lekhnitskii, S.G., 1963. Theory of an Anisotropic Elastic Body. Holden-Day, San Francisco.

Lim, W., Choi, S.Y., Sankar, B.V., 2001. Biaxial load effects on crack extension in anisotropic solids. Eng. Fract. Mech. 68, 403–416.

Manh, N.D., Evgrafov, A., Gersborg, A.R., Gravesen, J., 2011. Isogeometric shape optimization of vibrating membranes. Comput. Methods Appl. Mech. Eng. 200, 1343–1353.

Melenk, J., Babuska, I., 1996. The partition of unity finite element method: basic theory and applications. Comput. Methods Appl. Mech. Eng. 139, 289–314.

Menk, A., Bordas, S.P.A., 2010. Numerically determined enrichment functions for the extended finite element method and applications to bi-material anisotropic fracture and polycrystals. Int. J. Numer. Methods Eng. 83 (7), 805–828.

Merle, R., Dolbow, J., 2002. Solving thermal and phase change problems with the extended finite element method. Comput. Mech. 28, 339–350.

Moës, N., Gravouil, A., Belytschko, T., 2002. Non-planar 3D crack growth by the extended finite element and level sets-Part I: mechanical model. Int. J. Numer. Methods Eng. 53 (11), 2549–2568.

Mohammadi, S., 2008. Extended Finite Element Method for Fracture Analysis of Structures. Blackwell, UK.

Mohammadi, S., 2012. XFEM Fracture Analysis Of Composites. John Wiley & Sons, New Delhi, India.

Motamedi, D., Mohammadi, S., 2010. Dynamic analysis of fixed cracks in composites by the extended finite element method. Eng. Fract. Mech. 77 (17), 3373–3393.

Motamedi, D., Mohammadi, S., 2010. Dynamic crack propagation analysis of orthotropic media by the extended finite element method. Int. J. Fract. 161 (1), 21–39.

Murakami, Y.e., 1987. Stress Intensity Factors Handbook. Pergamon Press, Oxford.

Nguyen-Xuan, H., Thai, H., Nguyen-Thoi, T., 2013. Isogeometric finite element analysis of composite sandwich plates using a higher order shear deformation theory. Compos. Part B 55, 558–574.

Nobile, L., Carloni, C., 2005. Fracture analysis for orthotropic cracked plates. Compos. Struct. 68 (3), 285–293.

Ozturk, M., Erdogan, F., 1999. The mixed mode crack problem in an inhomogeneous orthotropic medium. Int. J. Fract. 98, 241–261.

Prasad, N.N.V., Aliabadi, M.H., Rooke, D.P., 1994a. Incremental crack growth in thermoelastic problems. Int. J. Fract. 66 (3), R45–R50.

Prasad, N.N.V., Aliabadi, M.H., Rooke, D.P., 1994b. The dual boundary element method for thermoelastic crack problems. Int. J. Fract. 66, 255–272.

Qian, X., 2010. Full analytical sensitivities in NURBS based isogeometric shape optimization. Comput. Methods Appl. Mech. Eng. 199, 2059–2071.

Qian, X., Sigmund, O., 2011. Isogeometric shape optimization of photonic crystals via coons patches. Comput. Methods Appl. Mech. Eng. 200, 2237–2255.

Raveendra, S.T., Banerjee, P., 1992. Boundary element analysis of cracks in thermally stresses planar structures. Int. J. Solids Struct. 29, 2301–2317.

Schovanec, L., Walton, J.R., 1988. On the order of the stress singularity for an anti-plane shear crack at the interface of two bonded inhomogeneous elastic materials. J. Appl. Mech. 55 (1), 234–236.

Shih, C.F., M, B., Nakamura, T., 1986. Energy release rate along a three-dimensional crack front in a thermally stressed body. Int. J. Fract. 30, 79–102.

Sih, G., Paris, P.C., Irwin, G.R., 1965. On cracks in rectilinearly anisotropic bodies. Int. J. Fract. Mech. 1, 189–203.
Stolarska, M., Chopp, D.L., Mos, N., Belytschko, T., 2001. Modelling crack growth by level sets in the extended finite element method. Int. J. Numer. Methods Eng. 51 (8), 943–960.
Sukumar, N., Moës, N., Moran, B., Belytschko, T., 2000. Extended finite element method for three-dimensional crack modelling. Int. J. Numer. Methods Eng. 48 (11), 1549–1570.
Sukumar, N., Chopp, D.L., Moës, N., Belytschko, T., 2001. Modeling holes and inclusions by level sets in the extended finite-element method. Comput. Methods Appl. Mech. Eng. 190, 6183–6200.
Sukumar, N., Chopp, D.L., Moran, B., 2003. Extended finite element method and fast marching method for three-dimensional fatigue crack propagation. Eng. Fract. Mech. 70 (1), 29–48.
Tada, H., Paris, P.C., Irwin, G.R., 2000. The Stress Analysis of Cracks Handbooks. ASME press, New York.
Temizer, I., W, P., Hughes, T., 2011. Contact treatment in isogeometric analysis with NURBS. Comput. Methods Appl. Mech. Eng. 200, 1100–1112.
Temizer, I., Wriggers, P., Hughes, T., 2012. Three-dimensional mortar-based frictional contact treatment in isogeometric analysis with NURBS. Comput. Methods Appl. Mech. Eng. 209–212, 115–128.
Thai Chien, H., Nguyen-Xua, H., Nguyen-Thanh, N., Le, T.-H., Nguyen-Thoi, T., 2012. Static free vibration and buckling analysis of laminated composite Reissner–Mindlin plates using NURBS-based isogeometric approach. Int. J. Numer. Methods Eng. 91, 571–603.
Thai Chien, H., Nguyen-Xuan, H., Bordas, S., Nguyen-Thanh, N., Rabczuk, T., 2012. Isogeometric analysis of laminated composite plates using the third-order shear deformation theory. Mech. Adv. Mater. Struct. (in press).
Thai Chien, H., Ferreira, A.J., Carrera, E., Nguyen-Xuan, H., 2013. Isogeometric analysis of laminated composite and sandwich plates using a layerwise deformation theory. Compos. Struct. 104, 196–214.
Tran, L.V., Thai, Chien H., Nguyen-Xuan, H., 2013. An isogeometric finite element formulation for thermal buckling analysis of functionally graded plates. Finite Elem. Anal. Des. 73, 65–76.
Tran Loc, V., Ferreira, A.J., Nguyen-Xuan, H., 2013. Isogeometric approach for analysis of functionally graded plates using higher-order shear deformation theory. Compos. Part B 51, 368–383.
Uhm, T., Youn, S., 2009. T-spline finite element method for the analysis of shell structures. Int. J. Numer. Methods Eng. 80 (4), 507–536.
Valizadeh, N., Natarajan, S., Gonzalez-Estrada, O.A., Rabczuk, T., Bui, T.Q., Bordas, S., 2013. NURBS-based finite element analysis of functionally graded plates: static bending, vibration, buckling and flutter. Compos. Struct. 99, 309–326.
Viola, A., Piva, A., Radi, E., 1989. Crack propagation in an prthotropic medium under general loading. Eng. Fract. Mech. 34 (5), 1155–1174.
Wall, W.A., Frenzel, M.A., Cyron, C., 2008. Isogeometric structural shape optimization. Comput. Methods Appl. Mech. Eng. 197, 2976–2988.
Wang, S.S., Yau, J.F., Corten, H.T., 1980. A mixed mode crack analysis of rectiliniear anisotropic solids using conservation laws of elasticity. Int. J. Fract. 16, 247–259.
Wilson, W.K., Yu, I.-W., 1979. The use of the J-integral in thermal stress crack problems. Int. J. Fract. 15, 377–387.
Yao, X.F., Xu, W., Arakawa, K., Takahashi, K., Mada, T., 2005. Dynamic optical visualization on the interaction between propagating crack and stationary crack. Opt. Lasers Eng. 43 (2), 195–207.